Intracellular Biodegradation of Ag Nanoparticles, Storage in Ferritin, and Protection by a Au Shell for Enhanced Photothermal Therapy

Ana Espinosa, Alberto Curcio, Sonia Cabana, Guillaume Radtke, Matthieu Bugnet, Jelena Kolosnjaj-Tabi, Christine Péchoux, Carmen Alvarez-Lorenzo, Gianluigi Botton, Amanda Pinto Da Silva, et al.

▶ **To cite this version:**

Ana Espinosa, Alberto Curcio, Sonia Cabana, Guillaume Radtke, Matthieu Bugnet, et al.. Intracellular Biodegradation of Ag Nanoparticles, Storage in Ferritin, and Protection by a Au Shell for Enhanced Photothermal Therapy. ACS Nano, 2018, 12 (7), pp.6523-6535. ⟨10.1021/acsnano.8b00482⟩. ⟨hal-01973569⟩

HAL Id: hal-01973569

https://hal.science/hal-01973569v1

Submitted on 31 Dec 2019

HAL is a multi-disciplinary open access archive for the deposit and dissemination of scientific research documents, whether they are published or not. The documents may come from teaching and research institutions in France or abroad, or from public or private research centers.

L'archive ouverte pluridisciplinaire **HAL**, est destinée au dépôt et à la diffusion de documents scientifiques de niveau recherche, publiés ou non, émanant des établissements d'enseignement et de recherche français ou étrangers, des laboratoires publics ou privés.

HAL Authorization

Intracellular Biodegradation of Ag Nanoparticles, Storage in Ferritin, and Protection by Au Shell for Enhanced Photothermal Therapy.

Ana Espinosa[†§], Alberto Curcio[†‖§], Sonia Cabana[‡ †‖], Guillaume Radtke[§], Matthieu Bugnet[⊥], Jelena Kolosnjaj-Tabi[†], Christine Péchoux[#], Carmen Alvarez-Lorenzo[‡], Gianluigi A. Botton[⊥], Amanda Silva[†], Ali Abou-Hassan[‖,] and Claire Wilhelm[†,]**

[†] Laboratoire Matière et Systèmes Complexes, UMR 7057, CNRS and University Paris Diderot, 75205 Paris cedex 13, France.

[‖] Sorbonne Université, CNRS, PHysico-chimie des Electrolytes et Nanosystèmes InterfaciauX, PHENIX, F-75005 Paris, France.

[‡]Departamento de Farmacología, Farmacia y Tecnología Farmacéutica, R+DPharma Group (GI-1645), Facultad de Farmacia and Health Research Institute of Santiago de Compostela (IDIS), Universidade de Santiago de Compostela, 15872 Santiago de Compostela, Spain

[§] Institut de Minéralogie, de Physique des Matériaux et de Cosmochimie (IMPMC), UMR 7590, CNRS, UPMC, 4 place Jussieu, 75005 Paris, France.

[⊥]Department of Materials Science and Engineering and Canadian Centre for Electron Microscopy, McMaster University, 1280 Main street West, Hamilton, ON, Canada L8S4M1.

[#] INRA, UR1196 GPL, MIMA2- Plateau de Microscopie Electronique 78352 Jouy-en-Josas, France.

§ AE and AC contributed equally to this work.

* Address correspondence to ali.abou_hassan@sorbonne-universite.fr and claire.wilhelm@univ-paris-diderot.fr

ABSTRACT

Despite their highly efficient plasmonic properties, gold nanoparticles are currently preferred to silver nanoparticles for biomedical applications such as photothermal therapy due to their high chemical stability in the biological environment. To confer protection while preserving their plasmonic properties, we allied the advantages of both materials and produced hybrid nanoparticles, made of an anisotropic silver nanoplate core coated with a frame of gold. The efficiency of such hybrid nanoparticles (Ag@AuNPs) in photothermia was compared to mono-metallic silver nanoplates (AgNPs) or gold nanostars (AuNPs). The structural and functional properties of AuNPs, AgNPs and Ag@AuNPs were investigated in environments of increasing complexity, in water suspensions, in cells, and in tumors *in vivo*. While AgNPs showed the greatest heating efficiency in suspension (followed by Ag@AuNPs and AuNPs), this trend was reversed intracellularly within a tissue-mimetic model. In this set-up, AgNPs failed to provide consistent photothermal conversion over time, due to structural damage induced by the intracellular environment. Remarkably, the degraded Ag was found to be stored within the iron-storage ferritin protein. By contrast, the Au shell provided the Ag@AuNPs with total Ag bio-persistence. As a result, photothermal therapy was successful with Ag@AuNPs *in vivo* in a mouse tumor model, providing the ultimate proof on Au shell's capability to shield the Ag core from the harsh biological environment, and preserve their excellent heating properties.

KEYWORDS: Nanoparticles, Gold, Silver, Biodegradation, Ferritin, Photothermal therapy.

... and among them went bright-eyed Athene, holding the precious aegis which is ***ageless*** *and* ***immortal****: a hundred tassels of* ***pure gold*** *hang fluttering from it, tight-woven each of them, and each the worth of a hundred oxen*. **(Homer, *The Iliad*, 4.17)**

The fast-forward progress in nanoparticle design has led to high-performance nanomaterials, featuring complex architecture and improved chemical and physical properties, which opens promising possibilities in the theranostic field.[1] Nevertheless, while nanoparticles might exhibit an unrivaled theranostic potential in a test tube, their effect might be different (and/or quickly dismantled) once the nano-objects enter the cell or the organism.[2-4] Once *in vivo*, the biomolecules rapidly cover the surface of the nanoparticles, affecting nanoparticle identity perception by the cell. In this regard, the main question of the last decade was "what does the cell see?",[5] addressing how bodily proteins interact with nanoparticles and disguise them with a protein corona, which is crucial to the nanoparticles - cell interaction.[6-9]

The composition and role of the protein corona has been extensively studied. In a logical sequence, the next question is certainly "what does the cell process?". This question is probably the topical issue of the current and the following decade, and refers to the destructive effects of the intracellular environment. Inside the organism, the nano-objects should experience important chemical and/or structural changes due to the bioprocessing.[2-3] Besides, the pivotal role of such bioprocessing will also directly impact nanoparticles therapeutic performance. However, exploring quantitatively the biotransformation and biological persistence of nanoparticles including plasmonic ones after processing *in vivo* is still an unmet challenge.

State-of-the-art plasmonic nanoparticles paved the way for ultra-sensitive diagnosis,[10-12] catalysis[13] and therapeutics (*e.g.* photothermal therapy).[14-16] Among theranostic plasmonic nanoparticles, anisotropic gold nanoparticles are probably the most popular ones, displaying excellent photo-thermal conversion efficiency while withstanding degradation.[17] Silver nanoparticles, on the other hand, are also excellent plasmonic candidates, that can feature

sometimes a stronger plasmonic resonance than their gold counterparts.[18] However, they are generally regarded as unstable and prone to intense and rapid oxidation and subsequent structural degradation in simplified aqueous saline and biological media.[19-21]

At the increasing degree of complexity, on the cell[22-23] or organism level,[24-25] the studies assessing silver nanoparticles degradation and performance become increasingly complicated. On the cellular level, the biodegradation measures become strongly impaired by cell division and subsequent dilution of nanoparticles, which intertwines with nanoparticles bioprocessing and dissolution. In addition, silver nanoparticles biodegradation, bio-distribution, and elimination, together with the difficulty to distinguish between Ag nanoparticles and ionic silver with common analytical methods, make it uneasy to retrieve a reliable bioprocessing fingerprint and quantitative degradation index. Particular analytical methods are sometimes used to identify the biodegradation of AgNPs within the organisms. [22, 23] Be that as it may, the rare available studies in cells,[22-23] isopods,[26] rodents,[24] and humans[25] converge to the same finding: silver nanoparticles rapidly dissolve.

Motivated by the high plasmonic potential of silver nanoparticles,[11, 19, 27] strategies have thus been developed to try to preserve Ag nanostructures from degradation.[28] Some of the strategies include surface modification of Ag nanostructures with an extra protecting layer of inorganic or organic material, such as silica,[23, 29-30] silica@titania double shells,[31] and self-assembled monolayers (SAMs) of organic thiols.[32] Despite the intricacy of the chemistry underlying the nanoparticles creation, only partial and short-term protection of silver could be achieved. Another strategy for protecting the unstable nanoparticles cores involved gold coatings. Indeed, gold combines the specific interests due to its own plasmonic properties and a particularly slow dissolution *in vivo*. To date, however, only a few studies were published assessing the *in vivo* fate of gold and silver composite nanoparticles, consisting of a (more or less porous) gold shell and a (more or less abundant) silver core. These studies encompass the NIR-absorbing hollow

Au-Ag nanoshells[33] and the NIR-absorbing Au nanoframes.[34] In these cases of nanoshells or nanoframes, which both exhibited a porous gold coating, the silver core rapidly dissolved. In Au nanoshells, an important dissolution and release of the silver from the core occurred within 24 hours from nanoshells injection to the mice. The dissolution and release of silver also occurred with gold nanoframes, yet to a lower extent, which was proportional to their lower content of Ag. Otherwise, the deposition of Au on Ag nanoparticles was proposed as an alternative method to provide bimetallic Au-Ag nanohybrids.[28, 35-38] This is only possible when complete coverage can be achieved by epitaxial growth of gold on silver, yet this still faces a number of technical challenges. Of the upper most is the galvanic replacement of Ag by Au atoms, resulting in oxidative etching and dissolution, giving rise to hollow structures.[39] Alternatively, very recently, Liu *et al*.[40] demonstrated the successful synthesis of Ag@Au nanohybrids using Ag nanoplates as templates, and sulfites as ligands and reducing agents for gold epitaxial growth, avoiding galvanic replacement, applicable to nanoparticles intended for use in SERS detection. Nevertheless, their photothermal potential and fate in the biological environment are yet unexplored.

The overriding aim of the present study was to synthesize a plasmonic nanohybrid with high absorbance in the near infrared (NIR) region, translating in a highly performant heat generation, and high stability in the biological environment. The methodological adjacent challenge was to provide quantitative methods to track the long-term intracellular fate of plasmonic nanoparticles.[41] To fulfil these requirements, anisotropic hybrids composed of a silver nanoplate core covered with a gold shell (Ag@AuNPs) were produced, and compared with state-of-the-art gold nanostars (AuNPs) and silver nanoplates (AgNPs). All share the same surface coating (polyvinylpyrolidone, PVP). Particular shapes were chosen to obtain a plasmon resonance in the NIR region.[42] Although the synthesis of gold nanoplates has been very recently reported,[43] the photochemical synthesis is difficult to reproduce and to elaborate in high

amounts for biomedical studies compared to the gold nanostars used herein. On the other side biocompatible silver nanostars synthesis with diameter below 100 nm is still missing in the literature. Thus we selected nanoparticles of different shapes (gold nanostars and silver nanoplates) which are the state-of-the-art efficient NIR absorbers available.

The heating efficiency was assessed in water and within a specific engineered-tissue model. The tissue was cultured for one month, and its cells (which did not divide and thus dilute the nanoparticles), processed the nanoparticles over time. Thermal measurements were applied to the tissue-mimetic model to determine the photothermal efficiency and the intracellular biodegradation status of the nanoparticles. The quantitative functional biotransformation index was also compared to qualitative proofs of morphological and chemical alterations over time by transmission electron microscopy (TEM) and scanning-TEM (STEM), coupled with elemental analysis. In such way we also managed to acquire plasmonic maps of the nanohybrids inside cells. Interestingly, we are demonstrating as well the involvement of the iron-storage protein ferritin in the storage of AgNPs degradation products. Finally, in the light of an antitumoral application, we assessed nanoparticles heating and therapeutic effects in tumor cells *in vitro*, and in tumor bearing mice *in vivo*, where the efficient photothermal therapy with Ag@AuNPs correlated with their biostability.

Two plasmonic metallic nanoparticles and a bi-metallic hybrid

Our first goal was to compare the heating efficiency of AuNPs, AgNPs and Ag@AuNPs in the same setting. To shift the plasmonic resonance to the NIR region in which tissue absorbance is minimal, nanomaterial design must be tailored to suit a tip shape or shell configuration. We thus selected and synthetized gold nanostars as leading representatives for AuNPs, silver nanoplates for AgNPs and silver nanoplates with a gold shell for Ag@AuNPs. Synthetized Au and Ag nanoparticles clearly featured star and prism-like shapes (Fig. 1A), with sizes of 77 ± 11 nm diameter and 47 ± 9 nm edge length for AuNPs and AgNPs, respectively. Ag@Au

hybrids were synthesized in an attempt to combines tip plasmons of Ag with an Au shell configuration. The resulting hybrids all exhibited a well-defined Au shell with truncated triangular nanoplate morphology. Au and Ag were present at a molar ratio of [Au]/[Ag]=2.5. The obtained average diameter measured by TEM was 57 ± 13 nm (composed of Ag prism-like core of 43 ± 8 nm in edge length and Au shell of 14 ± 5 nm). For all nanoparticles, plasmonic peaks were shifted in the NIR, centered at 700 nm, 680 nm, and 780 nm for AgNPs, Ag@AuNPs and AuNPs, respectively (Fig. 1B).

The heating efficiency was evaluated in water, at two concentrations (0.25 and 0.75 mM of Au, Ag, and Ag+Au), and at 680 nm wavelength and power density of 1 W/cm² (Fig. 1C). At the same molar concentration, heat generation increased from AuNPs to Ag@AuNPs (1.5-fold) and AgNPs (1.8-fold). This increase is even more impressive when heating potential is expressed in terms of the mass-renormalized specific absorption rate parameter (SAR, in W per g of material, *i.e.* Au or Ag). At a molar concentration of 0.25 mM, the SAR increased from 12.8 ± 1.8 kW/g_{Au} for AuNPs to 23.7 ± 1.7 kW/g_{Au+Ag} for Ag@AuNPs and 57.4 ± 4.1 kW/g_{Ag} for AgNPs. At 0.75 mM, SAR decreased to 8.9 ± 1.2 kW/g_{Au}, 14.8 ± 0.8 kW/g_{Ag+Au}, and 25.5 ± 2 kW/g_{Ag}, for AuNPs, Ag@AuNPs, and AgNPs, respectively, In line with the absorbance increase with concentration and subsequent SAR decrease in suspensions at higher nanoparticles concentrations.[44] AgNPs were thus the best performing photothermal agents followed by Ag@AuNPs and then AuNPs, when they are irradiated at 680 nm. Note that a simple model of light-to-heat energy transfer demonstrates that the SAR directly depends upon the absorbance A, according to SAR= $\frac{1}{m}.[I_0(1\text{-}10^{-A}).\eta]$, where m is the sample mass, Io(W) the laser power, and η the photothermal conversion efficiency, as described in detail elsewhere.[44-45] Then upon irradiation with the highest optical absorption wavelength for each nanoparticle (645, 705 and 760 nm for Ag@AuNPs, AgNPs, and AuNPs, respectively), the SAR will be increased by 23%, 2%, and 15% for Ag@AuNPs, AgNPs, and AuNPs,

respectively. The heating efficiency will still be maximal for AgNPs, followed by Ag@AuNPs, and then AuNPs.

Finally, surface plasmon maps, acquired using spatially-resolved electron energy-loss spectroscopy (EELS) for Ag and Ag@Au nanoplates, respectively, are shown on Figure 1D. They illustrate the corner (dipolar) mode of the Ag and Ag@Au nanoplates: at energies corresponding to the near infrared (1.4 eV for Ag and 1.9 for Ag@Au), hotspots are located on the tips of the triangles.[46-47] The large absorption centered at 680-700 nm (Fig. 1B) observed in UV-Vis-NIR is therefore clearly associated with the optical excitation of this mode in nanoplates.

A stem-cell derived tissue model incorporating the nanoparticles

All three plasmonic NPs thus appear eligible as photothermal agents, considering NP's potential to generate heat, based on the measurements obtained in water. However, when plasmonic agents' efficiency is evaluated for photothermal therapy, the performance assessments of the nano-heaters should be imperatively made in the intracellular medium. This intracellular measurement is pivotal, because the heat generation of nanoparticles depends on several parameters, including the aggregation state, the surrounding dielectric environment, and the refractive index close to the NP surface.[48] Even more importantly, measurements of the heating efficiency in aqueous environment do not take into account the intracellular stability. If Ag is assumed to undergo important structural modifications in the biological environment, while Au is expected to be highly resistant to any intracellular destabilization, these phenomena must be quantified in cells over several days / weeks. The rarity of such studies mainly stems from difficulties in performing long-lasting culture of cells having incorporated nanoparticles, while preventing cells division and nanoparticle dilution between daughter cells. To overcome this issue, we have developed a tissue model based on mesenchymal stem cells (MSC), assembled into a small spheroid, within which stem cells stop dividing, and start producing a collagen-rich

matrix, while remaining viable for months.[41, 49] Figure 2A shows spheroids at different time points over a one-month period. Here the spheroids were formed from stem cells having initially uptaken AuNPs, AgNPs, and Ag@AuNPs, at intracellular doses of 6.2 ± 1.2 pg of Au per cell, 2.4 ± 0.3 pg of Ag per cell, and 3.8 ± 1.4 pg of Au+Ag per cell, respectively. Figure 2A also shows large view TEM micrographs of such spheroids at day 25. Nanoparticles were clearly identified within cells, inside intracellular endosomes, and a rich extracellular matrix was prominent in between the cells.

Thermal tissue measurements: dual metrics to correlate biodegradation and photothermal stability

Thermal measurements were then set-up at the single spheroid scale. Spheroids were transferred in small 500 µl tubes (15 µL total volume) and further exposed to laser. Measurements were performed on independent spheroids (n≥5) at each time-point (day 1, 4, 10 and 25). Typical infrared images and average temperature elevation are shown in Figure 2B, respectively. These results show that, while the heating efficiency was equivalent for all three NPs at first day (day 1), it rapidly decreased for AgNPs, but remained remarkably stable for both AuNPs and Ag@AuNPs. This quantitatively demonstrates the photothermal stability for AuNPs and Ag@AuNPs, and the destructive intracellular effect on the thermal efficiency of AgNPs. It is important to highlight the fact that all spheroids displayed the same heat temperature starting point in this experiment. This was intentionally imposed by tuning the incubation conditions in a pre-experiment. Besides, we can also obtain the SAR from these thermal measurements, for intracellular plasmonic NPs. As it could be expected, the SAR was constant over time for AuNPs and Ag@AuNPs, with values of SAR_{AuNP} = 7.7 ±0 .8 kW/g_{Au} and $SAR_{Ag@AuNP}$ = 13.9 ± 0.4 kW/g_{Ag+Au}, respectively. For AgNPs at day 1, the SAR was 22.0 ± 2.3 kW/g_{Ag}, dropping to 6.8 ± 2.7 kW/g_{Ag} at day 4, and 4.3 ± 0.9 kW/g_{Ag} at days 9 and 25. Remarkably, for all NPs,

the SAR measured within the tissue at day 1, matches the SAR measured in water (for the 0.75 mM range concentration).

Nanoscale follow-up of the structural and plasmonic fate

In the next step, the NP's fate was tracked within the tissue at the nanoscale and at different time points, to establish the effect of the bio-environment's impact on the NP structure. Intracellular AuNPs are shown in supplementary Fig. S1 over time. All AuNPs were systematically found within endosomes, regardless of the stage of tissue maturation time. High magnifications of AuNPs within endosomes evidenced the typical branched-like nanostar structures, which conserved their morphological features under all conditions (see also the zoom in Fig. 2A), attesting to Au resistance and robustness in withstanding the destructive intracellular environment.

The scenario totally changed in the case of in-tissue follow-up of AgNPs (Fig. 3 and supplementary Fig. S2). Some intact AgNPs were only observed within the endosomes at day 1. As soon as day 4, most of the structures inside the endosomes appeared highly degraded, as evidenced by changes in size and shape (supplementary Fig. S3). The AgNPs initially featuring prism geometry with 45-nm edges, were mostly replaced with small spherical dots featuring 5-7 nm in size. At days 11 and 25, the same spherical dots of 5-7 nm in size were still detected. Figure 3B shows the Ag elemental mapping at day 4. The latter clearly evidences that the small 5-7 nm nanoparticles are made up of silver. Among different proteins that could play a role in silver degradation, ferritins are among the best-qualified candidates. Apoferritin was often used as a "nanoreactor" for the synthesis of different nanoparticles, including metallic such as silver,[50] gold-silver alloy,[51] or others such as copper sulfides.[52] Besides, binding sites and nucleation sites of Ag(I) that contain methionine residues have been identified inside the ferritin cavity.[50] Silver growth is thus theoretically possible inside the ferritin cavity. Besides, the fact that the Ag-dots detected since day 4 correspond in size to the ferritin protein, and don't evolve

with time (same size at day 25), indicate that they probably involve ferritin proteins, loaded with silver ions released from the nanoparticles. Also worth mentioning, these observed dots are very similar to the ferritin ones described after iron oxide nanoparticles degradation.[49] Besides, immunostaining with anti-ferritin antibody revealed a remarkable overexpression of the ferritin protein in cells containing degraded silver as compared to control (Fig. 3D and supplementary Fig. S4 for other views). Finally, we monitored the expression of the ferritin genes coding for subunit L (FerrL) and subunit H (FerrH). Remarkably, both genes were overexpressed in response to silver intracellular degradation, in a similar manner to the overexpression found in response to biodegradation of iron oxide nanoparticles.[49] Taken together, these observations and results confirm the role of ferritins in storing silver degraded from nanoparticles. Interesting as well, EELS also evidenced significant amounts of nitrogen in the vicinity of degrading and degraded Ag nanoparticles, substantiating a protein-rich environment involved in nanoparticle degradation (Figs. 3B and 3C). Finally, Figure 3C also demonstrates that, at day 25, surface plasmons have been destroyed by the intracellular processing.

Regarding Ag@Au hybrids, the TEM images at different time points (Fig. 4A and supplementary Fig. S5) indicated a fate comparable to the AuNPs. Similar to AuNPs, Ag@Au hybrids were confined within endosomes during the entire course of tissue maturation, remaining unchanged even at day 25. The elemental maps of both Ag and Au further confirmed these observations. Importantly, the maps show that the Au shell of the Ag@AuNPs succeeded in shielding of the Ag core against the harsh intracellular environment, regardless the time point, demonstrating that the Ag core of the hybrids survived degradation. Consistently, there was no evidence of small ferritin-like nano-structures within cells, nor accumulation of nitrogen within the endosomes (N could not be detected in the datasets). This non-detection of nitrogen also reflects the fact that the quantities of bodily proteins adsorbed on the surface of the nanoparticles

are below EELS's nitrogen detection threshold. Taken together, TEM and STEM analysis of Ag@AuNPs in cells over time closely matched photo-thermal stability data obtained at the tissue scale. Such a protection by Au shell can be likened to iron core protection by Au shell in magneto-plasmonics core@shell hybrids.[41, 53] This long-term intracellular stability was also confirmed by nanoplasmonic maps, which were obtained within endosomes at day 25 of tissue maturation, and showed a strong surface plasmon resonance (SPR) in the NIR (1.9 eV), further proof of the plasmonic stability of the Ag@AuNPs (Fig. 4D). To date, the SPR of NPs has been widely exploited in intracellular biodetection[54-55] using the SERS effect. In contrast, *in situ* monitoring of the SPR in simple or more complex media, such as *in cellulo,* has only started to be explored. Very recently Wang *et al*.[56] used dark field microscopy to follow at the intracellular level the shift in plasmon frequency of the scattering spectrum of Au-Ag alloy nanoboxes that etched in the presence of a cyanide analyte. Since the pioneering works who demonstrated that high resolution electron energy-loss spectroscopy (EELS) can allow 2D direct mapping of plasmon modes,[47, 57] to the best of our knowledge, 2D mapping of intracellular plasmon modes using EELS, as we provide herein, has not yet been reported.

NP structure and function fate *in vivo*: therapeutic translation to tumor model

The quiescent tissue model used was a strategical choice to manage the long-term NP quantitative biodegradation follow-up. Since cancer cells are constantly dividing, the assessment of such quantitative data is biased by the quick dilution of the nanoparticle intracellular content between daughter cells, intertwined with nanoparticle intracellular degradation. Both processes act in concert, rendering it difficult to ascertain their individual contribution. The quiescent tissue model, in which cells remain in a non-dividing state, set aside replication effect on cell dilution allowing isolating the sole contribution of degradation process. Nevertheless, cancer cells and *in vivo* tumor model enhance the degree of the bio-environment complexity, and provide a disease-relevant setting to test the photothermal effect

of these nanoheaters. First, Figures 5A and 5B show the *in vitro* cancer cell uptake (in pg per cell) of Ag and Ag@AuNPs, and the subsequent heating of half million cells, respectively. In line with the results observed for the stem cells, the hybrid Ag@AuNPs were more prone to enter the cells. As a consequence, for the same extracellular dose provided, the cellular heating was much more efficient for Ag@AuNPs. Second, Figure 5B also shows that, 24 hours after the incubation, the heating efficiency was conserved for Ag@AuNPs, but not for AgNPs, as applied for the tissue model. We then evaluated the therapeutic cytotoxicity efficiency of each nanoparticle by applying 1-min laser treatment (680nm; 1 W/cm²). Treatment was dose-dependent, resulting in 30% and 80% cell death for incubation dose at [Ag+Au]=15 and 30 µM of Ag@AuNPs. The same treatment efficiency was obtained regardless whether the cells were exposed right after incubation with the nanoparticles (2 hours) or 24 hours after. By contrast, for AgNPs, when exposure was applied 2 hours after incubation, only 10% and 30% of cell death was observed, for higher doses of [Ag]=30 and 90 µM, respectively. 24 hours later, therapy was even further decreased, with only the 90 µM dose resulting in a detectable cell death of only 15%. These cytotoxicity evaluations demonstrate that Ag@AuNPs are advantageous agents for photothermal therapy, while the poor stability of AgNPs dramatically limits their therapeutic assets.

We next monitored the photothermal heating the first days after intratumoral injection, and compared the value of temperature elevation for different mice ($n \geq 5$) right after injection (2 hours after), or 24 or 72 hours after. Figure 5D shows typical IR images of AgNP heating efficiency at both days, together with the average quantification of temperature elevation. Heating efficiency notably decreased 24 hours after injection. By contrast, when the same measurements were carried out for Ag@AuNPs (see Figures 5D and 5E for representative infrared images), we observed a conservation of heating 24 hours and 72 hours after injection. These measurements were done on tumor never heated, using a laser power of 1 W/cm², and

the temperatures measured 24 hours after injection were in the 45°C range for Ag@AuNP, and 40°C for AgNPs. To achieve higher temperature, we also performed the heating at 2 W/cm², similar to other *in vivo* preclinical studies involving PTT. The temperatures obtained 24 hours after injection attained about 55°C for Ag@AuNPs, but were still in the 45°C range for AgNPs.

A photothermal therapy investigation was conducted next, for AgNPs and Ag@AuNPs, with 10 minutes treatments, performed 24 hours and 48 hours after injection, with laser powers of 1 and 2 W/cm² (five groups of 4/5 mice each: two groups for AgNPs, two groups for Ag@AuNPs, plus control). Tumor growth was monitored each day for 12 days after the intratumoral nanoparticles injection (Figure 5G), and at the end of the 12 days, mice were sacrificed and excised tumors were weighted (Figure 5H). Therapy was very efficient for Ag@AuNPs at 2W/cm² laser exposure, resulting in almost total tumor regression. By contrast, tumor growth was only slowed down when animals were treated with AgNPs, following the same procedure. At a laser power of 1 W/cm², the treatment was slightly efficient only with Ag@AuNPs, but not with AgNPs.

Finally, to confirm their biostability *in vivo,* Ag@AuNPs were further observed by TEM (Fig. 5I) and STEM (Fig. 5J), at first day of injection, and 10 days after (see also supplementary Fig. S6). At day 0, Ag@AuNPs were found mostly within the tumoral extracellular matrix, or being internalized in first endocytotic vesicles (Fig. 5I (left)). At day 10, in all observed areas, Ag@AuNPs were localized within endosomes inside tumor cells (Figs. 5I (right) and supplementary Fig. S6), and the integrity of the bimetallic structure was remarkably conserved, the Ag core being systematically detected by STEM in all hybrids (Fig. 5J). These data provide the ultimate proof *in vivo* that strengthen *in vitro* observation on Au shell capability to shield the Ag core from the harsh biological environment, protecting its structural integrity and preserving ultra-efficient heating functional properties.

CONCLUSIONS

In a head-to-head comparison, the aim of this study was to rival plasmonic nano-heaters in order to assess their compliance to the harsh biological environment in terms of photothermal efficiency and intracellular stability. Gold nanostars (AuNPs) and silver nanoplates (AgNPs) were selected as state-of-the-art efficient NIR photothermal agents. The challenging strategy was to provide the Ag plate-like core with a gold shell (Ag@AuNPs) in the two-fold purpose to confer protection while maintaining excellent plasmonic and photothermal efficiency in the bio-environment. Structural and functional heating properties of AuNPs, AgNPs and Ag@AuNPs were thus investigated at increasing complexity levels from the NP suspension to the organism. In water, the evaluation of the heating efficiency for the different NPs in suspension revealed that AgNPs are the best performing ones followed by Ag@AuNPs and then AuNPs. This trend was reversed when measurements were carried out in the intracellular medium within a tissue-mimetic model. AgNPs experienced a massive intracellular biodegradation implicating the iron-storage ferritin protein, and resulting in an almost total loss of their photothermal efficiency, while AuNPs and Ag@AuNPs where structurally undamaged, and therefore maintained their enhanced photothermal efficiency. This was further demonstrated by testing their therapeutic potential *in vivo*, resulting in an almost total tumor regression with Ag@AuNPs, but low efficacy with AgNPs. The core@shell design of Ag@AuNPs thus empowers a biostable and efficient plasmonic hybrid photothermal agent.

METHODS

Chemicals

Silver nitrate (99%), gold (III) chloride trihydrate ($HAuCl_4$), sodium citrate tribasic dehydrate (98%), H_2O_2 (30 wt%), sodium borohydride (99%), gold (III) chloride hydrate (99%), sodium hydroxide (99%), sodium sulfite (98%), ascorbic acid, poly(vinylpyrrolidone) (M_w 10, 29 and 40 kDa), anhydrous ethanol and *N*,*N*-dimethylformamide (DMF) were purchased from *Sigma Aldrich* (France). All aqueous solutions were prepared using purified milliQ water.

Synthesis of plasmonic nanoparticles

Ag nanoplates (AgNPs). To obtain 45 nm-edge length Ag nanoplates, 50 mL of $AgNO_3$ (0.1 mM), 0.6 mL of trisodium citrate (30 mM), 1.5 mL of PVP (3.5 mM, M_w 29000), 120 µL of H_2O_2 (30 wt%) and 500 µL of $NaBH_4$ (100 mM) freshly prepared were mixed under magnetic stirring during 2 hours following the previous reported protocol of Métraux *et al*.[58] The resulting solution was centrifuged at 11000 rpm for 10 minutes and redispersed with ultrasound in water. The solution was covered with aluminum foil and stored at room temperature.

Au nanoparticles (AuNPs). Au nanostars were synthesized in two steps according to the seed-growth method described by Barbosa *et al*.[59] with some modifications.

- Gold seeds: 15 ± 0.2 nm citrate stabilized gold nanoseeds were first obtained by adding 5 mL of 1%wt sodium citrate aqueous solution to a boiling aqueous solution of HAuCl4 (100 mL, 0.5 mM) under continuous stirring and allowing to react for 30 min. The citrate stabilized seeds were modified using PVP (10 kDa) to provide 60 molecules/nm^2. The mixture was left overnight to complete ligand exchange. The suspension was centrifuged (7000 rpm; 40 min), the supernatant was discarded and the pellet was redispersed in anhydrous ethanol to a final gold concentration 3.5 mM.

- Growth of gold nanostars : We scaled up the described synthesis of Barbosa *et al*.[59] from 15 mL to 100 mL. An aqueous solution of $HAuCl_4$ (546 µL, 50 mM) was mixed with a solution of PVP (100 mL, 10 mM) in DMF. The mixture was stirred until complete disappearance of the

Au^{+3} CTTS band at 325 nm, followed by rapid addition of 800 µL of gold seeds in ethanol under vigorous stirring resulting in the formation of 75 nm of diameter. The color of the solution changes from colorless to blue within 40 min, indicating the formation of gold nanostars. The samples were centrifuged three times and redispersed in water.

Ag@AuNPs hybrids (Ag@AuNPs). Ag@AuNPs core/shell structures were prepared in three steps, following a well-established seeded growth approach described previously.[40] Firstly, 0.2 mL of $AgNO_3$ (0.1 M), 12 mL of trisodium citrate (0.075 M) and 0.48 mL of H_2O_2 (30 wt%) were diluted up to 200 mL with milliQ degassed water under stirring, to obtain Ag nanoplates solution. Then, 1.2 mL of fresh $NaBH_4$ (0.1 M) was quickly injected into the solution under vigorous stirring. After 1h and bubbles disappeared, 40 mL of the resulting solution were centrifuged at 11000 rpm for 8 minutes and redispersed in 2 mL of milliQ water. Secondly, the growth solution of Au is prepared by sequentially adding 40 µL of $HAuCl_4$ (0.25 M), 240 µL of NaOH (0.2 M) and 3 mL of Na_2SO_3 (0.01 M) to 4.72 mL of milliQ water using a vortex. The resulting solution was left undisturbed overnight and covered it with aluminum foil before used. Finally, 1 mL of PVP (5 wt%, M_w 40 kDa), 200 µL of fresh L-AA (0.5 M), 200 µL of NaOH (0.5 M), 50 µL of Na_2SO_3 (0.1 M) and 4 mL of the growth solution of Au were added sequentially to 2.55 mL of milliQ water. Then, 2 mL of Ag nanoplates were added to the solution to initiate the seeded growth. The reaction was then allowed to proceed undisturbed at room temperature for 6 h. Finally, Ag@Au nanoplates were collected by centrifugation at 8300 g during 10 minutes and washed two times with 7.5 mL of ethanol and redispersed in milliQ water.

Cell internalization assays

Plasmonic nanoparticles, AuNPs, AgNPs, and Ag@AuNPs were internalized and monitored in two biological environments: i) in a tissue model based on mesenchymal stem cells (MSC) for

long-lasting cell maturation and ii) in a tumor cell model based on human prostate cancer cells (PC-3 cells).

i) **Tissue model**: MSC cells were cultured until confluence in T75 flasks at 37 °C with 5% CO_2 in MSCBM medium (Lonza). They were labelled for 4 hours at the following concentration in complete culture medium: [Ag] = 60 µM for AgNPs, [Au] = 7.5 µM for AuNPs and [Ag+Au] = 15 µM for Ag@AuNPs. After incubation period, cells were washed three times with culture medium and detached by means of trypsin-EDTA solution. Cells were divided in four pellets of same number of cells (500 000 cells) and centrifuged at 1000 rpm. They were further placed at 37°C for tissue maturation over time with a specific medium composed of serum-free DMEM containing dexamethasone (*Sigma Aldrich*), sodium pyruvate (final concentration 1 mM), ascorbic acid-2 phosphate (*Sigma Aldrich*, final concentration 50 µM), L-proline (*Sigma Aldrich*, 0,35 mM), ITS Premix (*BD Biosciences*, 1/100 dilution) and TGF-□3 at 10 ng/mL. The medium was renewed every 3-4 days.

After 24 hours, the pellet started to shrink and form a three-dimensional cellular *spheroid* with *tissue*-like features. At day 1, 4, 10 and 25 of maturation, the spheroids were collected, fixed and kept in PBS for elemental characterization and electron microscopy imaging.

ii) **Tumor model**: PC-3 cells were cultivated in 6-well plates in Dulbecco's modified Eagle's medium (DMEM) supplemented with 5% fetal bovine serum (FBS) and 1% penicillin, and maintained at 37°C with 5% CO_2 until confluence. Cells were incubated with AgNPs, and Ag@AuNPs at the following concentrations: [Ag] = 15, 30 and 60 µM for AgNPs and [Ag+Au] = 7.5, 15 and 30 µM of Ag@AuNPs. The incubation times were 2 and 24 hours. Cells were collected by centrifugation (1200 rpm, 4 min). The cells were resuspended and fixed with glutaraldehyde (2.5%) at 4°C solution for one hour before storage in 30 µL cacodylate buffer for later measurements.

The Ag and/or Au load per cell was determined at the end of the incubation period by ICP-AES.

Characterization techniques

Transmission electron microscopy (TEM). TEM images of nanoparticles in aqueous dispersion were obtained by using a JEOL 100 CX instrument (100 kV) (UPMC, Paris, France) and a FEI-Philips TECNAI 12 (ImagoSeine, Institute Jaques Monod, Paris, France).

TEM micrographs of plasmonic nanoparticles in cells were obtained using a Zeiss EM 902 Hitachi HT7700 operating at 80 kV (MIMA2 platform, INRA, Jouy-en-Josas, France). After fixation protocols, the samples (spheroids and pellets) were then contrasted with Oolong Tea Extract (OTE) 0.5% in 0.1 M Na cacodylate buffer, post-fixed with 1% osmium tetroxide containing 1.5% potassium cyanoferrate for 1 h at room temperature, before finally being included in Epon resin after dehydration.

Elemental analysis. The concentrations of the Ag and Au content in aqueous dispersion were measured by Atomic Absorption Spectroscopy (AAS). Element content in cells was obtained by elemental analysis using an ICP-AES spectrometer (iCAP 6500, Thermo). The samples were digested in concentrated HNO_3 and recovered with a 1% HCl solution.

UV-Vis-NIR spectroscopy. The absorbance of plasmonic nanoparticles was measured using UV-Vis-NIR spectrometer (50 scan Cary, *Varian*) in the 300-1100 nm spectral range.

Photothermal effect measurements. 680 nm laser (*Laser Components S.A.S*) with an adjustable power up to 5 W was used to activate photothermal effect on samples. Nanomaterials in aqueous dispersion and *in vitro* in MSC and PC-3 cells contained in a 0.5-mL tube were illuminated with a power laser at 1 W/cm^2. Temperature elevation was recorded using an infrared thermal imaging camera (*FLIR SC7000*).

Scanning transmission electron microscopy (STEM). A drop of nanoparticles aqueous dispersions was deposited onto an ultrathin carbon film on a holey carbon support grid (Ted Pella Inc.). Ultrathin sections (40 nm) of nanoparticles internalized in cells were cut, deposited on lacey carbon film 200 Mesh copper grids. Chemical maps were acquired in Electron Energy Loss Spectroscopy (EELS) using the Spectrum Imaging technique in Scanning Transmission Electron Microscopy (STEM) on a FEI Titan Cubed 80-300, operated at 200 kV, equipped with a *Gatan* GIF Quantum electron energy loss spectrometer, and with spherical aberration correctors of the probe and image lenses.

Immunofluorescence of ferritin. MSC cells cultured on glass coverslips were fixed with 4% PFA (Interchim) for 10 min at room temperature, 7 days after incubation with AgNPs and Ag@AuNPs. After washing with PBS, cells were permeabilized with PBS-Triton X-100 (0.2% v/v) for 10 min. Nonspecific sites were blocked with 5% (w/v) bovine serum albumin (BSA) diluted in PBS-Triton X-100 (0.1% v/v) during 2 hours and incubated overnight at 4 °C with anti-ferritin primary antibody (EPR3004Y, Abcam) diluted 1:100 in 1% BSA PBS-Triton X-100 (0.1% v/v). After several PBS washings, the Alexa Fluor 488-conjugated antirabbit IgG secondary antibody (A32731, Thermo Fisher) diluted 1:500 in 1% BSA PBS was incubated for 1 h at room temperature. Cells were washed with PBS and their nuclei were stained with DAPI diluted 1:1000 in PBS for 20 min at room temperature and mounted with a drop of Fluoromount (Sigma-Aldrich). Cells were analyzed with an Olympus JX81/BX61 device/Yokogawa CSU device spinning-disk microscope (Andor Technology), equipped with a 63X oil objective (Olympus).

Gene expression quantification by real-time PCR. Total RNA was extracted using NucleoSpin RNA II kit (Macheney-Nagel) according to manufacturer's instruction. Reverse transcription into cDNA was achieved using SuperScript II reverse transcriptase (Invitrogen) according to the manufacturer's instructions. qPCR was performed with StepOnePlus (Applied

Biosystems) using the SYBR Green reagent (Applied Biosystems). The expression of reference gene RPLP0 was used as a reference transcript. The sequences of primers used are:

RPLP0 fwd: 5′ TGC ATC AGT ACC CCA TTC TAT CAT 3′

RPLP0 rev: 5′ AAG GTG TAA TCC GTC TCC ACA GA 3′

FerrL fwd: 5′ CGA ATT GGC CGA GGA GAA 3′

FerrL rev: 5′ GCC ACG CTG GTT TTG CAT 3′

FerrH fwd: 5′ TG GCT TGG CGG AAT TTC TGT 3′

FerrH rev: 5′ GC CCG AGG CTT AGC TTT CAT 3′

***In vitro* cytotoxicity assay.** After internalization of AgNPs and Ag@AuNPs by PC3 cells, followed by 1 min heating at 1W/cm², the cytotoxicity measurement was carried out 24 h after the photothermal treatment consisting in 1 min heating with 680 nm laser at 1W/cm². The metabolic Alamar Blue assay (Invitrogen) was used to detect live cells, according to the supplier instruction. Briefly, the culture medium was replaced by DMEM without phenol red, supplemented with 10% Alamar blue, and incubated with the cells for 1 hour. 200 µl were then transferred to 96-well plate and analysed with plate reader (Enspire Perkin Elmer, excitation 570 nm, detection 580 nm). All analyses were normalized by the average value obtained with control non-treated cells.

***In vivo* photothermal effect.** *In vivo* studies using AgNPs and Ag@AuNPs were carried out using 6 weeks old male immunodeficient nude NMRI mice weighing 20 ± 1 g, provided by *Janvier Laboratories* (France). They were hosted in the facilities of Animalerie Buffon, Institute Jacques Monod, Paris, France. Animal experiments were approved by Buffon Ethics committee (project reference CEB-07-2016).

The NMRI tumor-bearing nude mice were prepared by inoculating cells (2×10^6 PC-3 human prostate carcinoma cells in 100 µL of physiological saline (PBS) in the left and right flanks. Tumors were allowed to grow for about two or three weeks, when the volume was

approximately 125 mm^3. AgNPs and Ag@AuNPs saline dispersion at 0.75 mM of [Ag] and [Ag+Au], respectively. Twenty-three tumors in 12 animals were divided into several groups: 10 tumors were injected with AgNPs tumors, 11 tumors injected with Ag@AuNPs and 3 non-injected tumors served as controls.

The tumors were irradiated with a 680 laser at 1 W/cm^2 for 1 min on days 1 and 4 post-injection. The photothermal heating was monitored with an infrared thermal camera (FLIR SC7000) for each laser. Animals were anesthetized with ketamine/xylazine during the measurements.

Mouse tumors were collected and cut into 1-mm^3 pieces, fixed with 2% glutaraldehyde in 0.1 M sodium cacodylate buffer and kept in 0.1 M sodium cacodylate and 0.2 M sucrose buffer. After they were prepared in thin sections (40 nm) for TEM and STEM observation.

In vivo photothermal therapy

In vivo therapy was performed on 12 animals bearing 22 tumors. The tumors were divided as follows: 9 tumors were injected with AgNPs, 9 tumors with Ag@AuNPs and 4 non-injected tumors served as controls.

The tumors were irradiated with a 680 nm laser at 1 W/cm^2 (n=4) and at 2 W/cm^2 (n=5) for 10 min on days 1 and 2 post-injection. Animals were anesthetized with isofluorane during the injections and during the treatments. The animals were sacrificed 12 days after the treatment or before the tumor reached 1 cm^3. Tumor volume was measured every day, with a caliper and calculated from the formula $V = \text{length} \times \text{width} \times \text{height} \times \pi / 6$. After sacrifice at day 12, all tumors were harvested and weighed.

SUPPORTING INFORMATION

Additional figures. This material is available free of charge *via* the Internet at http://pubs.acs.org.

AUTHOR INFORMATION

Corresponding Authors

*E-mails: ali.abou_hassan@upmc.fr; claire.wilhelm@univ-paris-diderot.fr

Author Contributions

The manuscript was written through contributions of all authors. All authors have given approval to the final version of the manuscript.

ACKNOWLEDGEMENTS

The tissular biodegradation part of this work was supported by the European Council (ERC-2014-CoG project MaTissE 648779). The *in vivo* photothermal evaluation was supported by the European Union (Marie Curie Intra-European Project FP7-PEOPLE-2013-740 IEF-62647 and), by Paris city (Research in Paris). STEM analysis was supported by the Natural Sciences and Engineering Research Council (NSERC), Canada. The authors acknowledge the staff of Animalerie Buffon facilities, Institute Jacques Monod, Paris, and thank Aurore Van de Walle and Nathalie Luciani for fruitful discussions.

FIGURES

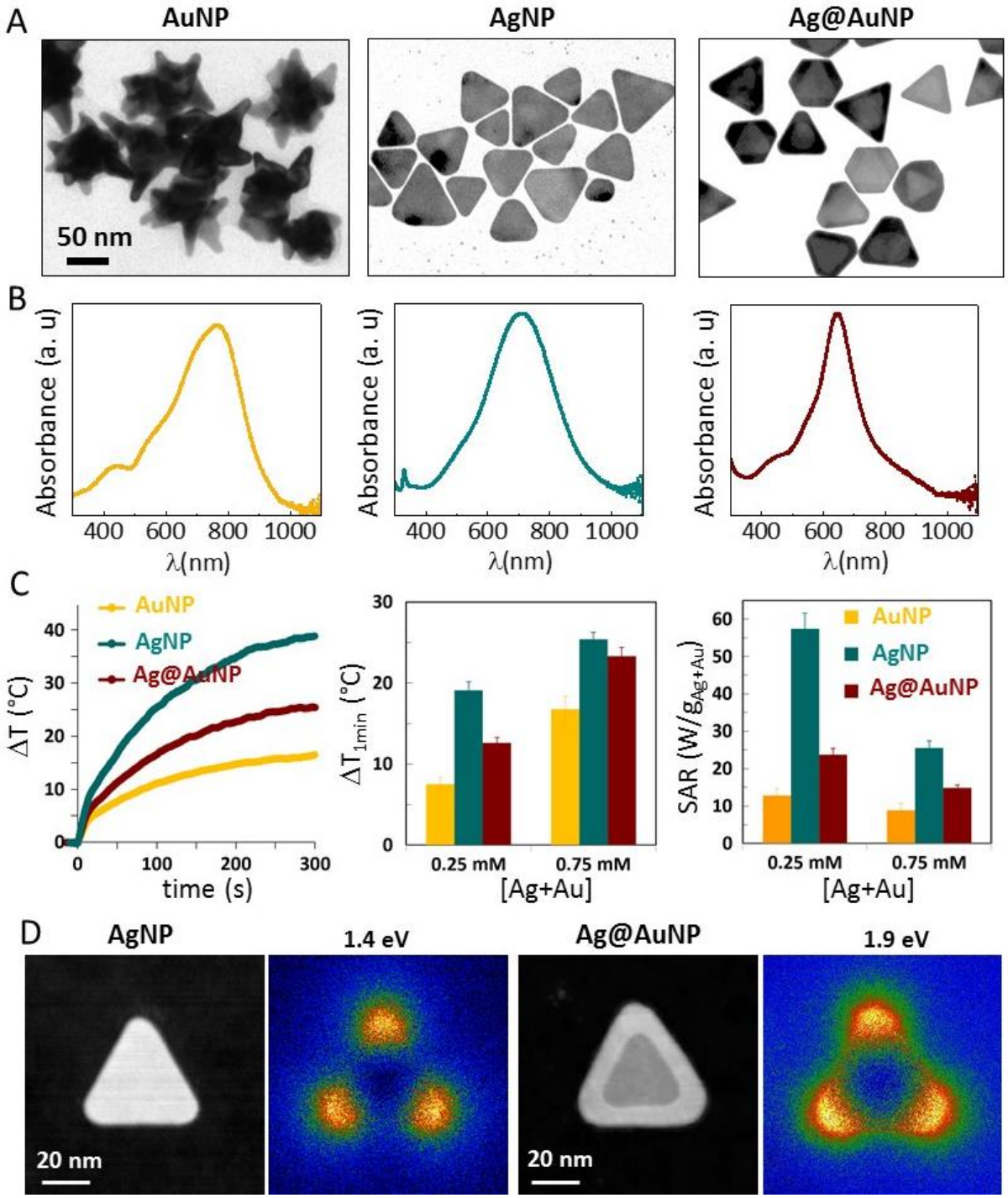

Figure 1. Au, Ag and Ag@Au photothermal nanoparticles. (**A**) Transmission electron microscopy (TEM) images and (**B**) UV-Vis-NIR spectra of AuNPs, AgNPs and Ag@AuNPs dispersed in water. (**C**) Temperature elevation profile (left) of the three NPs at 0.25 mM of [Au], [Ag] and [Ag+Au] under 680 nm laser irradiation (680 nm, 1 W/cm²); Average temperature elevation after 1 min of laser irradiation (middle) for solutions at 0.25 mM and

0.75 mM of [Au], [Ag] and [Ag+Au]; Average SAR (in W per grams of Au, Ag and Ag+Au, right) (**D**) Annular dark field (ADF) STEM micrograph (left) and EELS plasmon resonance maps (right) of the corner (dipolar) mode of Ag and Ag@Au nanoprisms, at 1.4 eV and 1.9 eV, respectively. Note that the difference between the average resonance centered at 680-700 nm in the UV-Vis-NIR spectrum and the energy of mode imaged in EELS in a single isolated nanoprism is primarily related to the size, shape and thickness distribution of these nanoparticles.

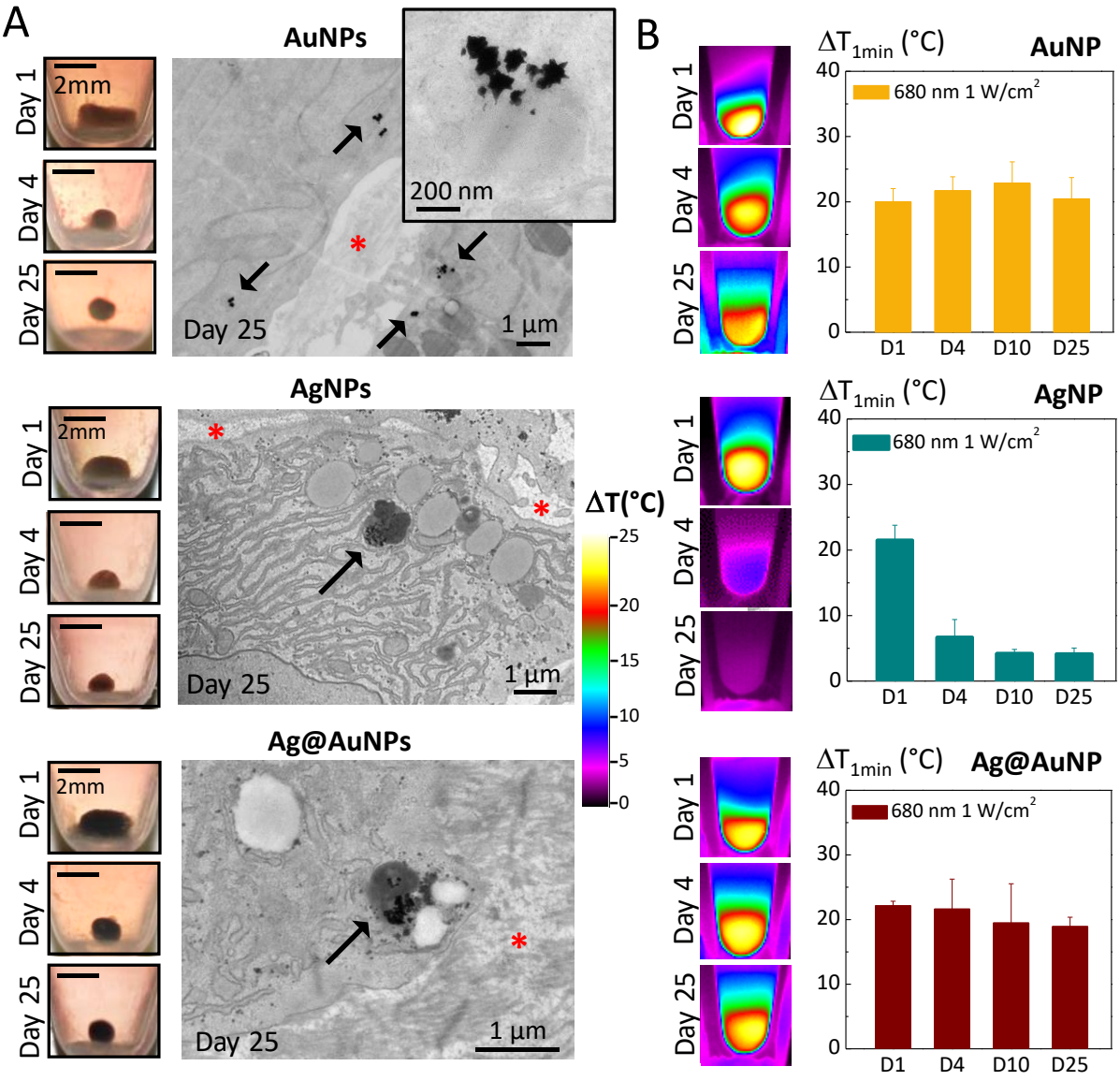

Figure 2. Intracellular biodegradation assessment in model tissue. (**A**) Images (left) of the spheroids composed of human mesenchymal stem cells (MSC, 500 000 cells) labelled with AuNPs, AgNPs and AgAuNPs. Images are shown on day 1, 4 and 25 of tissue maturation. Spheroid size reduction over time is due to compacting of cell tissue. TEM micrographs (right) of the spheroids core structure at day 25. The nanoparticles are confined into endosomes (arrows). Endosome containing nanoparticles is zoomed for AuNPs, evidencing an intact star-branched structure at day 25. Red stars denote the rich extracellular matrix secreted by the cells within the model tissue (**B**) Infrared thermal images (left) of typical stem cells spheroids after 1 min of laser irradiation at 680 nm and 1 W/cm² over time: day 1, 4 and 25 after incubation with AuNPs, AgNPs and Ag@AuNPs. Temperature elevation (right) averaged over multiple independent spheroids ($n \geq 5$) at day 1, 4, 10 and 25 for the different nanoparticles. The heating capability is similar for all NPs at day 1 after cell internalization, but it declines quickly for AgNPs. Photothermal properties remain stable over time for AuNPs and Ag@AuNPs.

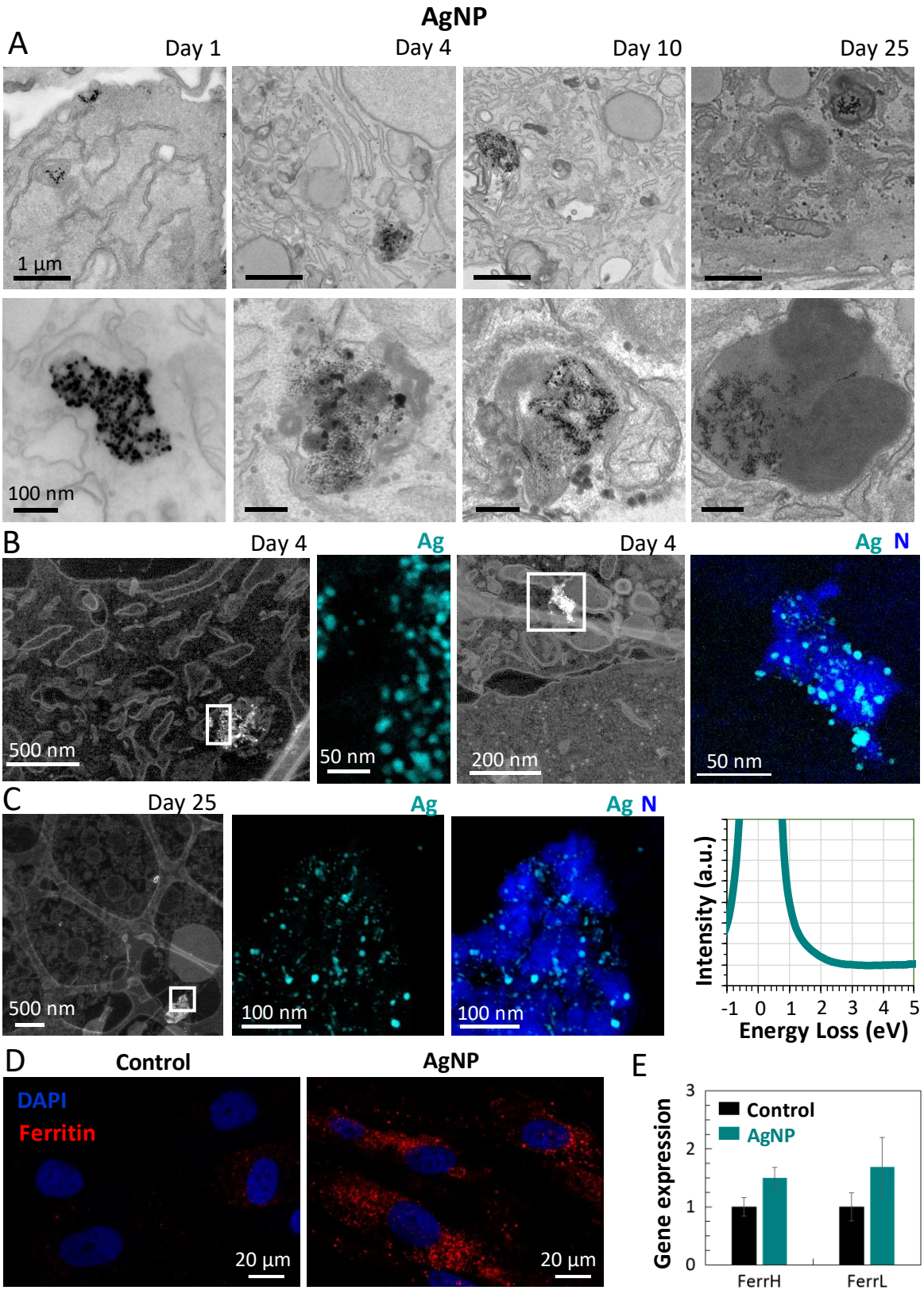

Figure 3. One-month intracellular monitoring of AgNPs within the tissue. (**A**) TEM images of AgNPs in the cellular environment at different magnifications on days 1, 4, 10 and 25 after internalization in MSC stem cells. At day 1, Ag nanoprisms are already deteriorated and are

confined inside endosomes, which are massively degraded from day 4 over time (days 10 and 25), with a change of shape to 5-7 nm spherical particles ferritin-like. (**B**) Annular dark field (ADF) image and EELS elemental maps of AgNPs at day 4 inside the endosomes. Right image shows that nitrogen (N) is abundant and diffused inside the endosome evidencing degradation process. Note that these elemental maps have been obtained by multiple linear least-squares fit of the EELS spectrum-image using reference spectra for N-K and Ag-M_{45} edges acquired in the same conditions. This procedure was necessary as these edges substantially overlap in energy. (**C**) At day 25: ADF image, EELS elemental maps and representative low energy-loss spectrum recorded at day 25 (from the boxed area in the Ag, N map) highlighting the absence of major plasmon resonances in the near IR range. (**D**). Immunostaining (in red) of the ferritin protein in MSC cells at day 7, in control conditions (no NPs), or with internalized degraded AgNPs. Nuclear DAPI staining (in blue) is overlaid. (**E**). Relative expression level of genes coding for ferritin light chain (FerrL) and heavy chain (FerrH). Gene expression was measured at day 10 after AgNPs incubation with cells, normalized to reference gene RPLP0 and expressed relative to the average control value. Error bars represent the SEM.

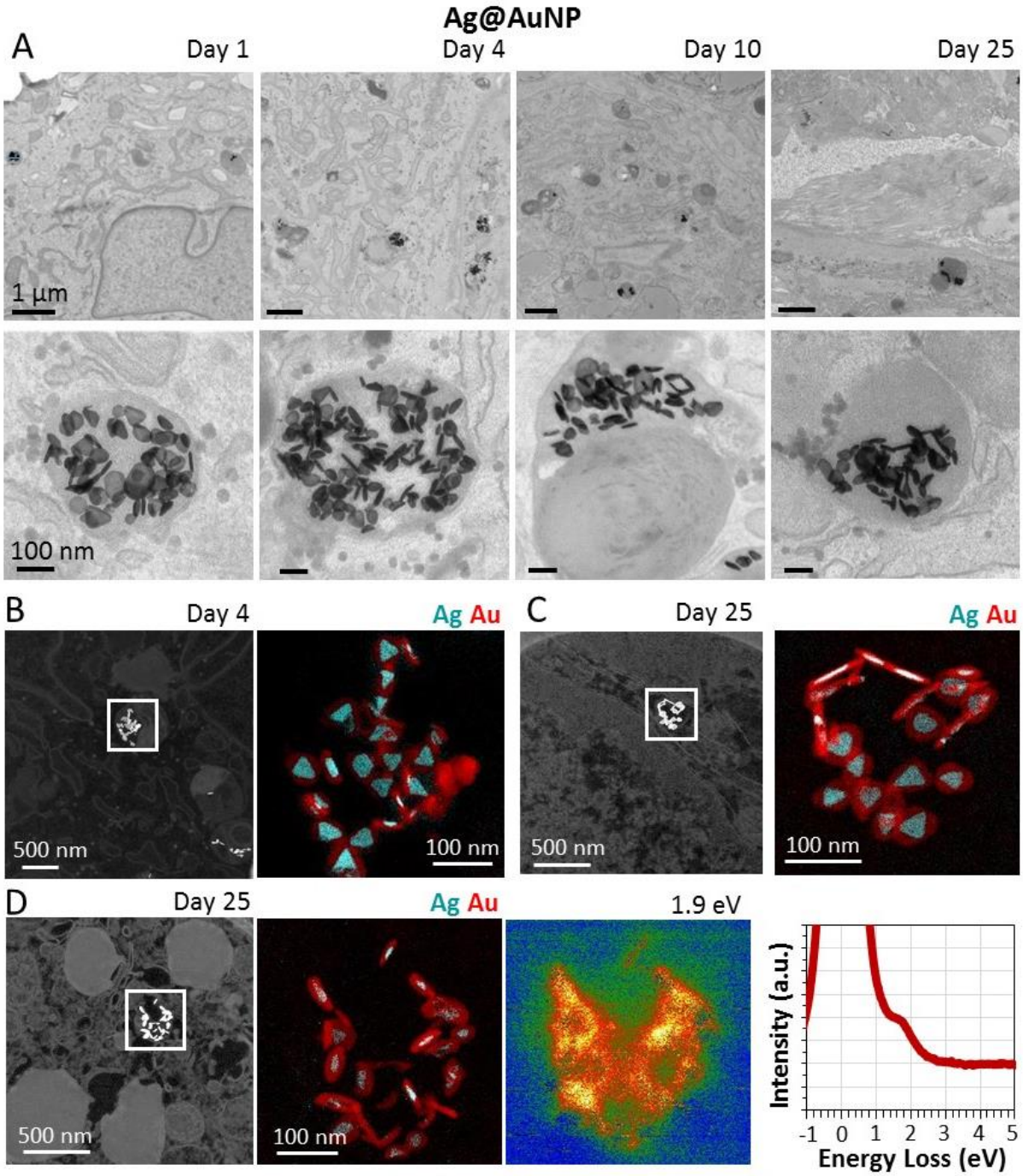

Figure 4. One-month intracellular monitoring of Ag@AuNPs within the tissue. (**A**) TEM images of Ag@AuNPs in the cellular environment at different magnifications on days 1, 4, 10 and 25 after internalization in MSC stem cells. From day 1 to 25, all nanoparticles are confined inside endosomes and their core-shell nanostructure is still maintained. (**B,C**) ADF image and EELS elemental maps (Ag,Au,N) at day 4 (**B**) and day 25 (**C**). (**D**) At day 25: For the same endosome (boxed area in the ADF image on the left), EELS elemental maps (Ag,Au) and

plasmon resonance maps at 1.9 eV. The average low energy-loss spectrum is also shown on the right, highlighting the major resonance at about 1.9 eV, for means of comparison with Figure 3C where no resonance was visible at this energy range.

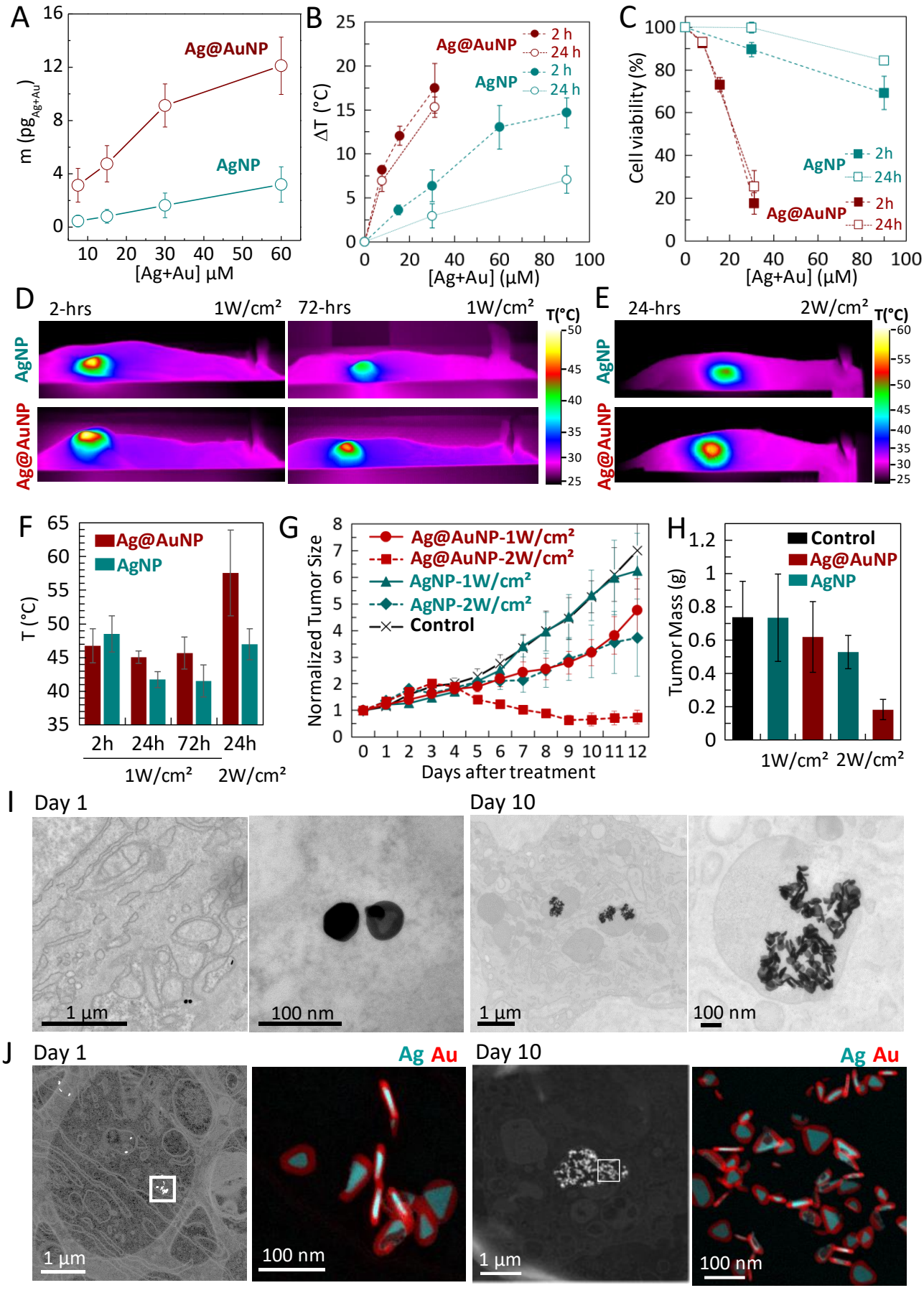
A
m (pg Ag+Au)
Ag@AuNP
AgNP
[Ag+Au] μM
B
ΔT (°C)
Ag@AuNP
AgNP
2 h
24 h
[Ag+Au] (μM)
C
Cell viability (%)
AgNP
Ag@AuNP
2h
24h
[Ag+Au] (μM)
D
2-hrs
1W/cm²
72-hrs
1W/cm²
T(°C)
AgNP
Ag@AuNP
E
24-hrs
2W/cm²
T(°C)
AgNP
Ag@AuNP
F
T (°C)
Ag@AuNP
AgNP
2h
24h
72h
24h
1W/cm²
2W/cm²
G
Normalized Tumor Size
Ag@AuNP-1W/cm²
Ag@AuNP-2W/cm²
AgNP-1W/cm²
AgNP-2W/cm²
Control
Days after treatment
H
Tumor Mass (g)
Control
Ag@AuNP
AgNP
1W/cm²
2W/cm²
I
Day 1
Day 10
1 μm
100 nm
1 μm
100 nm
J
Day 1
Ag Au
Day 10
Ag Au
1 μm
100 nm
1 μm
100 nm

Figure 5. AgNP and Ag@AuNP *in vitro* in tumor cells and *in vivo* in tumors. (**A**) ICP measurement of Ag and Au mass per cell within PC-3 tumor cell uptake. AgNP and Ag@AuNP were incubated for 2 h at 7.5 - 90 µM of [Ag] and [Ag+Au], respectively. (**B**) Temperature increase of PC-3 cells labelled with AgNP and Ag@AuNP after 1 min of 680-nm laser irradiation at 1 W/cm^2. Cells were incubated for 2-hours at different concentrations ([Ag] = 15-90 µM for AgNPs and [Ag+Au] = 7.5-30 µM for Ag@AuNPs). Laser exposure was performed either 2 hours after the end of the incubation, or 24 hours later. (**C**) Cytotoxicity induced by the 1-min laser exposure, performed either 2 hours after incubation, or 24 hours later, and measured by the Alamar metabolic test. (**D**) Infrared thermal images of mice injected with AgNPs and Ag@AuNPs at 0.75 mM of [Ag] and [Ag+Au], respectively, and exposed under NIR-laser irradiation (680 nm, 1 min, 1 W/cm^2) on injection day (2 hours), or 24 hours and 72 hours later. (**E**). Infrared thermal images of mice injected with same dose of AgNPs and Ag]AuNPs, and exposed to 680 NIR-laser for 1 min at 2 W/cm^2, 24 hours after injection. (**F**) Average temperature increase after 1 min of 680 nm NIR laser exposure, on tumors injected with 0.75 mM of AgNPs and Ag@AuNPs, and exposed 2 hours after injection (1 W/cm²), 24 hours (1 and 2 W/cm²), or 72 hours after (1 W/cm²). Note that to perform this thermal quantification, the tumors must not have been exposed before, to avoid any absorbing scar. (**G**) Normalized tumor size average in non-injected control mice, and mice injected with AgNPs and Ag@AuNPs, and treated with laser at 1 and 2 W/cm² for 10 minutes, 24 hours and 48 hours after injection. Tumor growth was monitored over 12 days after injection. **(H)** Mass of excised tumors at day 12 for the different groups. (**I,J**) TEM micrographs (I), ADF images and EELS elemental maps (J) of Ag@AuNPs at day 1 and 10 after intratumoral injection.

SYNOPSIS TOC

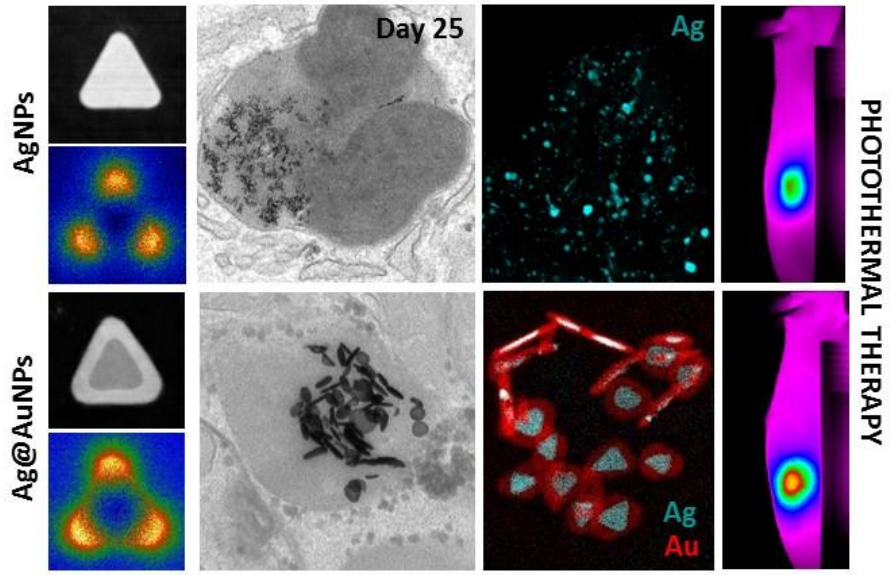

REFERENCES

1. Bogart, L. K.; Pourroy, G.; Murphy, C. J.; Puntes, V.; Pellegrino, T.; Rosenblum, D.; Peer, D.; Lévy, R., Nanoparticles for Imaging, Sensing, and Therapeutic Intervention. *ACS Nano* **2012,** *6*, 5961-5971.

2. Feliu, N.; Docter, D.; Heine, M.; del Pino, P.; Ashraf, S.; Kolosnjaj-Tabi, J.; Macchiarini, P.; Nielsen, P.; Alloyeau, D.; Gazeau, F.; Stauber, R. H.; Parak, W. J., *In Vivo* Degeneration and the Fate of Inorganic Nanoparticles. *Chem. Soc. Rev.* **2016,** *45*, 2440-2457.

3. Kreyling, W. G.; Abdelmonem, A. M.; Ali, Z.; Alves, F.; Geiser, M.; Haberl, N.; Hartmann, R.; Hirn, S.; De Aberasturi, D. J.; Kantner, K., *In Vivo* Integrity of Polymer-Coated Gold Nanoparticles. *Nat. Nanotech.* **2015,** *10*, 619-623.

4. Soenen, S. J.; Parak, W. J.; Rejman, J.; Manshian, B., (Intra) Cellular Stability of Inorganic Nanoparticles: Effects on Cytotoxicity, Particle Functionality, and Biomedical Applications. *Chem. Rev.* **2015,** *115*, 2109-2135.

5. Lynch, I.; Salvati, A.; Dawson, K. A., Protein-Nanoparticle Interactions: What Does the Cell See? *Nat. Nanotech.* **2009,** *4*, 546-547.

6. Monopoli, M. P.; Walczyk, D.; Campbell, A.; Elia, G.; Lynch, I.; Bombelli, F. B.; Dawson, K. A., Physical− Chemical Aspects of Protein Corona: Relevance to *in Vitro* and *in Vivo* Biological Impacts of Nanoparticles. *J. Am. Chem. Soc* **2011,** *133*, 2525-2534.

7. Vilanova, O.; Mittag, J. J.; Kelly, P. M.; Milani, S.; Dawson, K. A.; Rädler, J. O.; Franzese, G., Understanding the Kinetics of Protein–Nanoparticle Corona Formation. *ACS Nano* **2016,** *10*, 10842-10850.

8. Carril, M.; Padro, D.; del Pino, P.; Carrillo-Carrion, C.; Gallego, M.; Parak, W. J., In Situ Detection of the Protein Corona in Complex Environments. *Nat. Comm.* **2017,** *8*, 1542.

9. Ke, P. C.; Lin, S.; Parak, W. J.; Davis, T. P.; Caruso, F., A Decade of the Protein Corona. *ACS Nano* **2017,** *11*, 11773–11776.

10. Schlücker, S., Surface-Enhanced Raman Spectroscopy: Concepts and Chemical Applications. *Angew. Chem. Int. Ed.* **2014,** *53*, 4756-4795.

11. Lane, L. A.; Qian, X.; Nie, S., Sers Nanoparticles in Medicine: From Label-Free Detection to Spectroscopic Tagging. *Chem. Rev.* **2015,** *115*, 10489-10529.

12. Hu, J.; Sanz-Rodríguez, F.; Rivero, F.; Rodríguez, E. M.; Torres, R. A.; Ortgies, D. H.; Solé, J. G.; Alfonso, F.; Jaque, D., Gold Nanoshells: Contrast Agents for Cell Imaging by Cardiovascular Optical Coherence Tomography. *Nano Res.* **2017**, *11*, 676-685.

13. Zaleska-Medynska, A.; Marchelek, M.; Diak, M.; Grabowska, E., Noble Metal-Based Bimetallic Nanoparticles: The Effect of the Structure on the Optical, Catalytic and Photocatalytic Properties. *Adv. Colloid Interface Sci.* **2016,** *229*, 80-107.

14. Jaque, D.; Maestro, L. M.; Del Rosal, B.; Haro-Gonzalez, P.; Benayas, A.; Plaza, J.; Rodriguez, E. M.; Sole, J. G., Nanoparticles for Photothermal Therapies. *Nanoscale* **2014,** *6*, 9494-9530.

15. Rai, M.; Ingle, A. P.; Birla, S.; Yadav, A.; Santos, C. A. D., Strategic Role of Selected Noble Metal Nanoparticles in Medicine. *Crit. Rev. Microbiol.* **2016,** *42*, 696-719.

16. Maestro, L. M.; Haro-González, P.; Sánchez-Iglesias, A.; Liz-Marzán, L. M.; García Solé, J.; Jaque, D., Quantum Dot Thermometry Evaluation of Geometry Dependent Heating Efficiency in Gold Nanoparticles. *Langmuir* **2014,** *30*, 1650-1658.

17. Yang, X.; Yang, M.; Pang, B.; Vara, M.; Xia, Y., Gold Nanomaterials at Work in Biomedicine. *Chem. Rev.* **2015,** *115*, 10410-10488.

18. Le Ru, E.; Etchegoin, P., *Principles of Surface-Enhanced Raman Spectroscopy: And Related Plasmonic Effects*. Elsevier: 2008.

19. Li, J.-F.; Zhang, Y.-J.; Ding, S.-Y.; Panneerselvam, R.; Tian, Z.-Q., Core–Shell Nanoparticle-Enhanced Raman Spectroscopy. *Chem. Rev.* **2017,** *117*, 5002-5069.

20. Jiang, T.; Song, J.; Zhang, W.; Wang, H.; Li, X.; Xia, R.; Zhu, L.; Xu, X., Au–Ag@ Au Hollow Nanostructure with Enhanced Chemical Stability and Improved Photothermal Transduction Efficiency for Cancer Treatment. *ACS Appl. Mater. Interfaces* **2015,** *7*, 21985-21994.

21. Manshian, B. B.; Pfeiffer, C.; Pelaz, B.; Heimerl, T.; Gallego, M.; Möller, M.; Del Pino, P.; Himmelreich, U.; Parak, W. J.; Soenen, S. J., High-Content Imaging and Gene Expression Approaches to Unravel the Effect of Surface Functionality on Cellular Interactions of Silver Nanoparticles. *ACS Nano* **2015,** *9*, 10431-10444.

22. Caballero-Díaz, E.; Pfeiffer, C.; Kastl, L.; Rivera-Gil, P.; Simonet, B.; Valcárcel, M.; Jiménez-Lamana, J.; Laborda, F.; Parak, W. J., The Toxicity of Silver Nanoparticles Depends on Their Uptake by Cells and Thus on Their Surface Chemistry. *Part. Part. Syst. Charact.* **2013,** *30*, 1079-1085.

23. Jiang, X.; Miclăuş, T.; Wang, L.; Foldbjerg, R.; Sutherland, D. S.; Autrup, H.; Chen, C.; Beer, C., Fast Intracellular Dissolution and Persistent Cellular Uptake of Silver Nanoparticles in Cho-K1 Cells: Implication for Cytotoxicity. *Nanotoxicology* **2015,** *9*, 181-189.

24. Su, C.-K.; Liu, H.-T.; Hsia, S.-C.; Sun, Y.-C., Quantitatively Profiling the Dissolution and Redistribution of Silver Nanoparticles in Living Rats Using a Knotted Reactor-Based Differentiation Scheme. *Anal. Chem.* **2014,** *86*, 8267-8274.

25. Roman, M.; Rigo, C.; Castillo-Michel, H.; Munivrana, I.; Vindigni, V.; Mičetić, I.; Benetti, F.; Manodori, L.; Cairns, W. R., Hydrodynamic Chromatography Coupled to Single-Particle Icp-Ms for the Simultaneous Characterization of Agnps and Determination of Dissolved Ag in Plasma and Blood of Burn Patients. *Anal. Bioanal. Chem.* **2016,** *408*, 5109-5124.

26. Romih, T.; Jemec, A.; Kos, M.; Hočevar, S. B.; Kralj, S.; Makovec, D.; Drobne, D., The Role of Pvp in the Bioavailability of Ag from the Pvp-Stabilized Ag Nanoparticle Suspension. *Environ. Pollut.* **2016,** *218*, 957-964.

27. Di Corato, R.; Palumberi, D.; Marotta, R.; Scotto, M.; Carregal-Romero, S.; Rivera_Gil, P.; Parak, W. J.; Pellegrino, T., Magnetic Nanobeads Decorated with Silver Nanoparticles as Cytotoxic Agents and Photothermal Probes. *Small* **2012,** *8*, 2731-2742.

28. Gao, C.; Lu, Z.; Liu, Y.; Zhang, Q.; Chi, M.; Cheng, Q.; Yin, Y., Highly Stable Silver Nanoplates for Surface Plasmon Resonance Biosensing. *Angew. Chem. Int. Ed.* **2012,** *51*, 5629-5633.

29. Baida, H.; Billaud, P.; Marhaba, S.; Christofilos, D.; Cottancin, E.; Crut, A.; Lermé, J.; Maioli, P.; Pellarin, M.; Broyer, M., Quantitative Determination of the Size Dependence of Surface Plasmon Resonance Damping in Single Ag@ Sio2 Nanoparticles. *Nano Lett.* **2009,** *9*, 3463-3469.

30. Brandon, M. P.; Ledwith, D. M.; Kelly, J. M., Preparation of Saline-Stable, Silica-Coated Triangular Silver Nanoplates of Use for Optical Sensing. *J. Colloid Interface Sci.* **2014,** *415*, 77-84.

31. Wang, Y.; Chen, L.; Liu, P., Biocompatible Triplex Ag@ Sio2@ Mtio2 Core–Shell Nanoparticles for Simultaneous Fluorescence-Sers Bimodal Imaging and Drug Delivery. *Chem. Eur. J.* **2012,** *18*, 5935-5943.

32. Jiang, X.; Zeng, Q.; Yu, A., Thiol-Frozen Shape Evolution of Triangular Silver Nanoplates. *Langmuir* **2007,** *23*, 2218-2223.

33. Goodman, A. M.; Cao, Y.; Urban, C.; Neumann, O.; Ayala-Orozco, C.; Knight, M. W.; Joshi, A.; Nordlander, P.; Halas, N. J., The Surprising *in Vivo* Instability of near-Ir-Absorbing Hollow Au–Ag Nanoshells. *ACS Nano* **2014,** *8*, 3222-3231.

34. Wang, L.; Chen, Y.; Lin, H. Y.; Hou, Y.-T.; Yang, L.-C.; Sun, A. Y.; Liu, J.-Y.; Chang, C.-W.; Wan, D., Near-Ir-Absorbing Gold Nanoframes with Enhanced Physiological Stability and Improved Biocompatibility for *in Vivo* Biomedical Applications. *ACS Appl. Mater. Interfaces* **2017,** *9*, 3873-3884.

35. Aherne, D.; Charles, D. E.; Brennan-Fournet, M. E.; Kelly, J. M.; Gun'ko, Y. K., Etching-Resistant Silver Nanoprisms by Epitaxial Deposition of a Protecting Layer of Gold at the Edges. *Langmuir* **2009,** *25*, 10165-10173.

36. Shahjamali, M. M.; Bosman, M.; Cao, S.; Huang, X.; Saadat, S.; Martinsson, E.; Aili, D.; Tay, Y. Y.; Liedberg, B.; Loo, S. C. J., Gold Coating of Silver Nanoprisms. *Adv. Funct. Mater.* **2012,** *22*, 849-854.

37. Yang, Y.; Liu, J.; Fu, Z.-W.; Qin, D., Galvanic Replacement-Free Deposition of Au on Ag for Core–Shell Nanocubes with Enhanced Chemical Stability and Sers Activity. *J. Am. Chem. Soc* **2014,** *136*, 8153-8156.

38. Hobbs, K.; Cathcart, N.; Kitaev, V., Gold-Plated Silver Nanoparticles Engineered for Sensitive Plasmonic Detection Amplified by Morphological Changes. *Chem. Comm.* **2016,** *52*, 9785-9788.

39. Au, L.; Lu, X.; Xia, Y., A Comparative Study of Galvanic Replacement Reactions Involving Ag Nanocubes and Aucl2− or Aucl4−. *Adv. Mater.* **2008,** *20*, 2517-2522.

40. Liu, H.; Liu, T.; Zhang, L.; Han, L.; Gao, C.; Yin, Y., Etching-Free Epitaxial Growth of Gold on Silver Nanostructures for High Chemical Stability and Plasmonic Activity. *Adv. Funct. Mater.* **2015,** *25*, 5435-5443.

41. Mazuel, F.; Espinosa, A.; Radtke, G.; Bugnet, M.; Neveu, S.; Lalatonne, Y.; Botton, G. A.; Abou-Hassan, A.; Wilhelm, C., Magneto-Thermal Metrics Can Mirror the Long-Term Intracellular Fate of Magneto-Plasmonic Nanohybrids and Reveal the Remarkable Shielding Effect of Gold. *Adv. Funct. Mater.* **2017,** *27*, 1605997.

42. Liu, A.; Wang, G.; Wang, F.; Zhang, Y., Gold Nanostructures with near-Infrared Plasmonic Resonance: Synthesis and Surface Functionalization. *Coord. Chem. Rev.* **2016**, *336*, 28-42.

43. Zhai, Y.; DuChene, J. S.; Wang, Y.-C.; Qiu, J.; Johnston-Peck, A. C.; You, B.; Guo, W.; DiCiaccio, B.; Qian, K.; Zhao, E. W., Polyvinylpyrrolidone-Induced Anisotropic Growth of Gold Nanoprisms in Plasmon-Driven Synthesis. *Nat. Mater.* **2016,** *15*, 889.

44. Jiang, K.; Smith, D. A.; Pinchuk, A., Size-Dependent Photothermal Conversion Efficiencies of Plasmonically Heated Gold Nanoparticles. *J. Phys. Chem. C* **2013,** *117*, 27073-27080.

45. Plan Sangnier, A.; Preveral, S.; Curcio, A.; K. A. Silva, A.; Lefèvre, C. T.; Pignol, D.; Lalatonne, Y.; Wilhelm, C., Targeted Thermal Therapy with Genetically Engineered Magnetite Magnetosomes@Rgd: Photothermia Is Far More Efficient Than Magnetic Hyperthermia. *J. Control. Release* **2018,** *279*, 271-281.

46. Pastoriza-Santos, I.; Liz-Marzán, L. M., Colloidal Silver Nanoplates. State of the Art and Future Challenges. *J. Mater. Chem.* **2008,** *18*, 1724-1737.

47. Nelayah, J.; Kociak, M.; Stéphan, O.; de Abajo, F. J. G.; Tencé, M.; Henrard, L.; Taverna, D.; Pastoriza-Santos, I.; Liz-Marzán, L. M.; Colliex, C., Mapping Surface Plasmons on a Single Metallic Nanoparticle. *Nat. Phys.* **2007,** *3*, 348.

48. Miller, M. M.; Lazarides, A. A., Sensitivity of Metal Nanoparticle Surface Plasmon Resonance to the Dielectric Environment. *J. Phys. Chem. B* **2005,** *109*, 21556-21565.

49. Mazuel, F.; Espinosa, A.; Luciani, N.; Reffay, M.; Le Borgne, R.; Motte, L.; Desboeufs, K.; Michel, A.; Pellegrino, T.; Lalatonne, Y.; Wilhelm, C., Massive Intracellular Biodegradation of Iron Oxide Nanoparticles Evidenced Magnetically at Single-Endosome and Tissue Levels. *ACS Nano* **2016,** *10*, 7627-7638.

50. Kasyutich, O.; Ilari, A.; Fiorillo, A.; Tatchev, D.; Hoell, A.; Ceci, P., Silver Ion Incorporation and Nanoparticle Formation inside the Cavity of Pyrococcus Furiosus Ferritin: Structural and Size-Distribution Analyses. *J. Am. Chem. Soc.* **2010,** *132*, 3621-3627.

51. Shin, Y.; Dohnalkova, A.; Lin, Y., Preparation of Homogeneous Gold− Silver Alloy Nanoparticles Using the Apoferritin Cavity as a Nanoreactor. *J. Phys. Chem. C* **2010,** *114*, 5985-5989.

52. Wang, Z.; Huang, P.; Jacobson, O.; Wang, Z.; Liu, Y.; Lin, L.; Lin, J.; Lu, N.; Zhang, H.; Tian, R., Biomineralization-Inspired Synthesis of Copper Sulfide–Ferritin Nanocages as Cancer Theranostics. *ACS Nano* **2016,** *10*, 3453-3460.

53. Espinosa, A.; Bugnet, M.; Radtke, G.; Neveu, S.; Botton, G. A.; Wilhelm, C.; Abou-Hassan, A., Can Magneto-Plasmonic Nanohybrids Efficiently Combine Photothermia with Magnetic Hyperthermia? *Nanoscale* **2015,** *7*, 18872-18877.

54. Taylor, J.; Huefner, A.; Li, L.; Wingfield, J.; Mahajan, S., Nanoparticles and Intracellular Applications of Surface-Enhanced Raman Spectroscopy. *Analyst* **2016,** *141*, 5037-5055.

55. Rodríguez-Lorenzo, L.; Krpetic, Z.; Barbosa, S.; Alvarez-Puebla, R. A.; Liz-Marzán, L. M.; Prior, I. A.; Brust, M., Intracellular Mapping with Sers-Encoded Gold Nanostars. *Integr. Biol.* **2011,** *3*, 922-926.

56. Wang, P.; Bai, Y.; Yao, C.; Li, X.; Zhou, L.; Wang, W.; El-Toni, A. M.; Zi, J.; Zhao, D.; Shi, L., Intracellular and *in Vivo* Cyanide Mapping *Via* Surface Plasmon Spectroscopy of Single Au–Ag Nanoboxes. *Anal. Chem.* **2017,** *89*, 2583-2591.

57. Colliex, C.; Kociak, M.; Stéphan, O., Electron Energy Loss Spectroscopy Imaging of Surface Plasmons at the Nanometer Scale. *Ultramicroscopy* **2016,** *162*, A1-A24.

58. Métraux, G. S.; Mirkin, C. A., Rapid Thermal Synthesis of Silver Nanoprisms with Chemically Tailorable Thickness. *Adv. Mater.* **2005,** *17*, 412-415.

59. Barbosa, S.; Agrawal, A.; Rodríguez-Lorenzo, L.; Pastoriza-Santos, I.; Alvarez-Puebla, R. A.; Kornowski, A.; Weller, H.; Liz-Marzán, L. M., Tuning Size and Sensing Properties in Colloidal Gold Nanostars. *Langmuir* **2010,** *26*, 14943-14950.

SUPPORTING INFORMATIONS

Intracellular Biodegradation of Ag Nanoparticles, Storage in Ferritin, and Protection by Au Shell for Enhanced Photothermal Therapy.

Ana Espinosa[†§], Alberto Curcio[†∥§], Sonia Cabana[‡ †∥], Guillaume Radtke[§], Matthieu Bugnet[⊥], Jelena Kolosnjaj-Tabi[†], Christine Péchoux[#], Carmen Alvarez-Lorenzo[‡], Gianluigi A. Botton[⊥], Amanda Silva[†], Ali Abou-Hassan[∥,] and Claire Wilhelm[†,*]*

[†] Laboratoire Matière et Systèmes Complexes, UMR 7057, CNRS and University Paris Diderot, 75205 Paris cedex 13, France.

[∥] Sorbonne Université, CNRS, PHysico-chimie des Electrolytes et Nanosystèmes InterfaciauX, PHENIX, F-75005 Paris, France.

[‡]Departamento de Farmacología, Farmacia y Tecnología Farmacéutica, R+DPharma Group (GI-1645), Facultad de Farmacia and Health Research Institute of Santiago de Compostela (IDIS), Universidade de Santiago de Compostela, 15872 Santiago de Compostela, Spain

[§] Institut de Minéralogie, de Physique des Matériaux et de Cosmochimie (IMPMC), UMR 7590, CNRS, UPMC, 4 place Jussieu, 75005 Paris, France.

[⊥]Department of Materials Science and Engineering and Canadian Centre for Electron Microscopy, McMaster University, 1280 Main street West, Hamilton, ON, Canada L8S4M1.

[#] INRA, UR1196 GPL, MIMA2- Plateau de Microscopie Electronique 78352 Jouy-en-Josas, France.

§ AE and AC contributed equally to this work.

* Address correspondence to ali.abou_hassan@sorbonne-universite.fr and claire.wilhelm@univ-paris-diderot.fr

AuNPs

Day 1

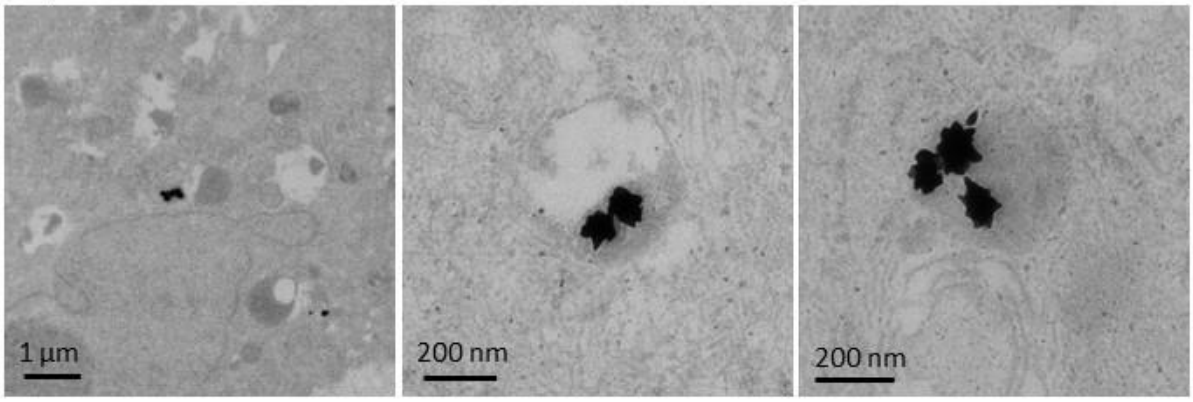

Day 4

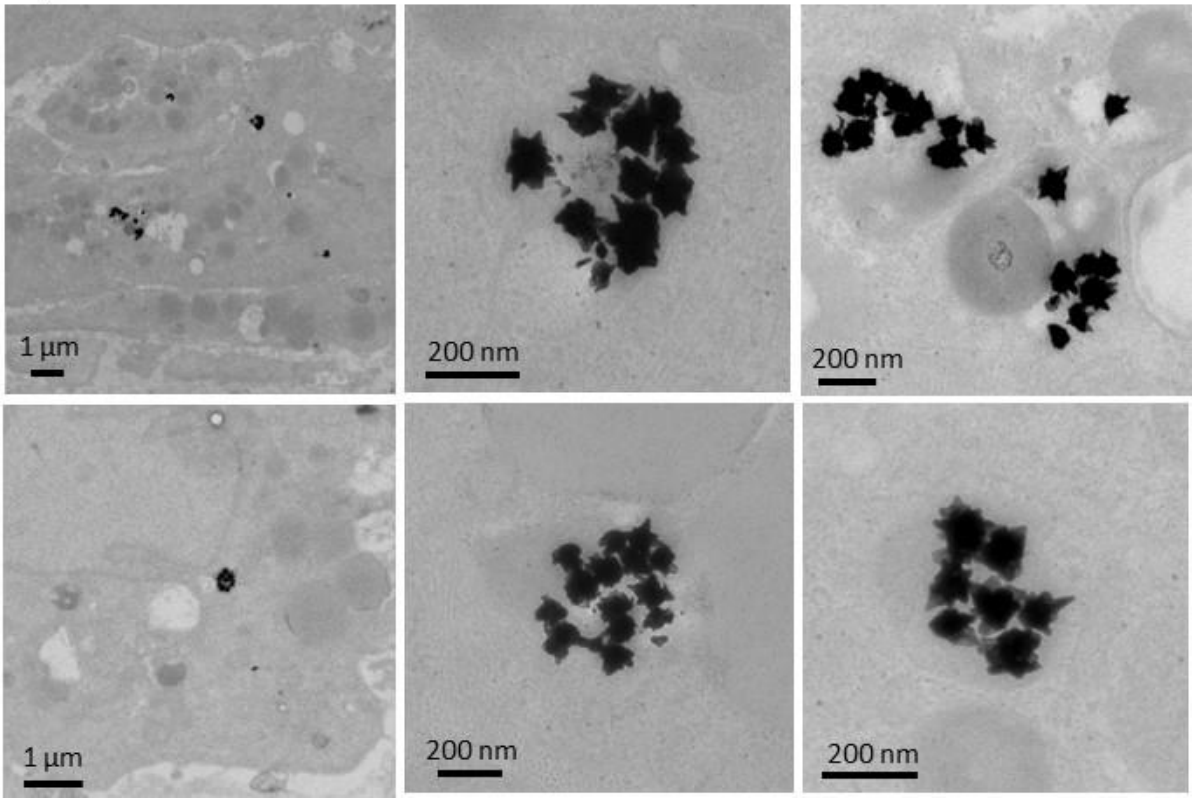

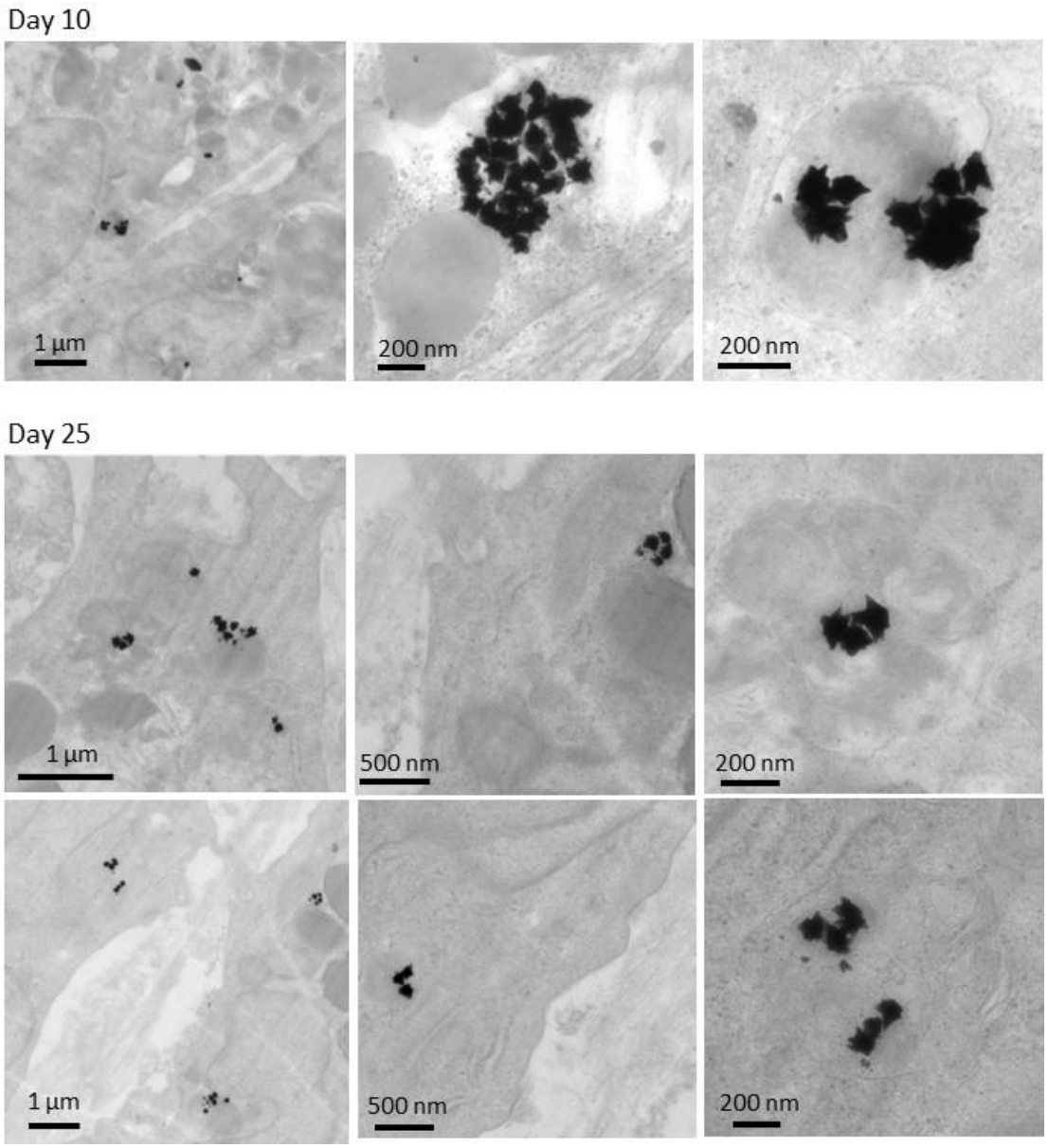

Figure S1. One-month intracellular monitoring of AuNPs within the tissue. TEM images of AuNPs in the cellular environment at different magnifications on days 1, 4, 10 and 25 after internalization in MSC stem cells. Branched-like nanostar structures remain intact over the time and they are confined in endosomes, as previously demonstrated in another study (at day 1)[1].

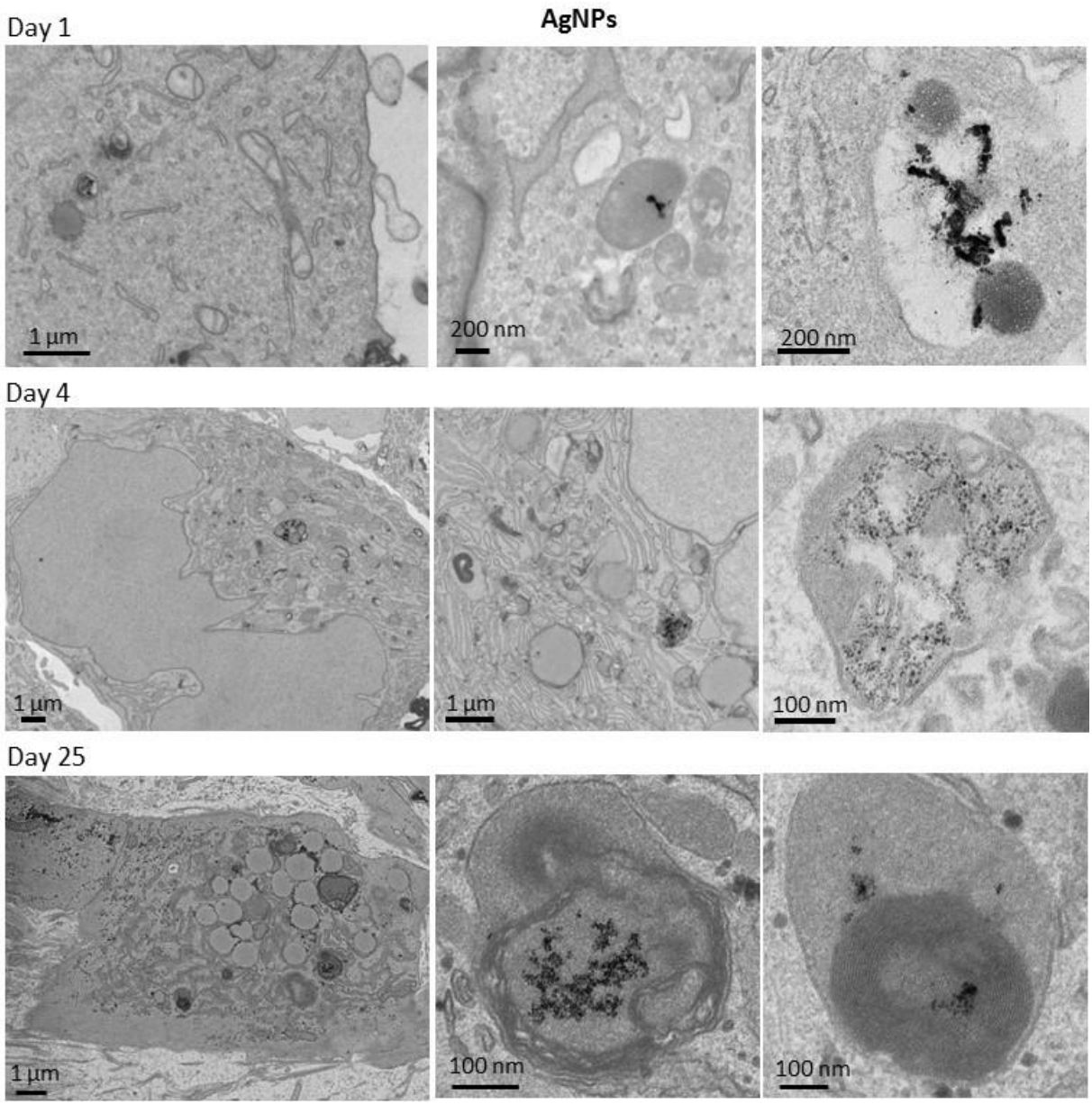

Figure S2. TEM micrographs of MSC stem cells on days 1, 4 and 25 after incubation with AgNPs. Micrographs were acquired at different magnifications (scale bars 1 µm and 100 nm), from whole cell level to zooms on intracellular endosomes.

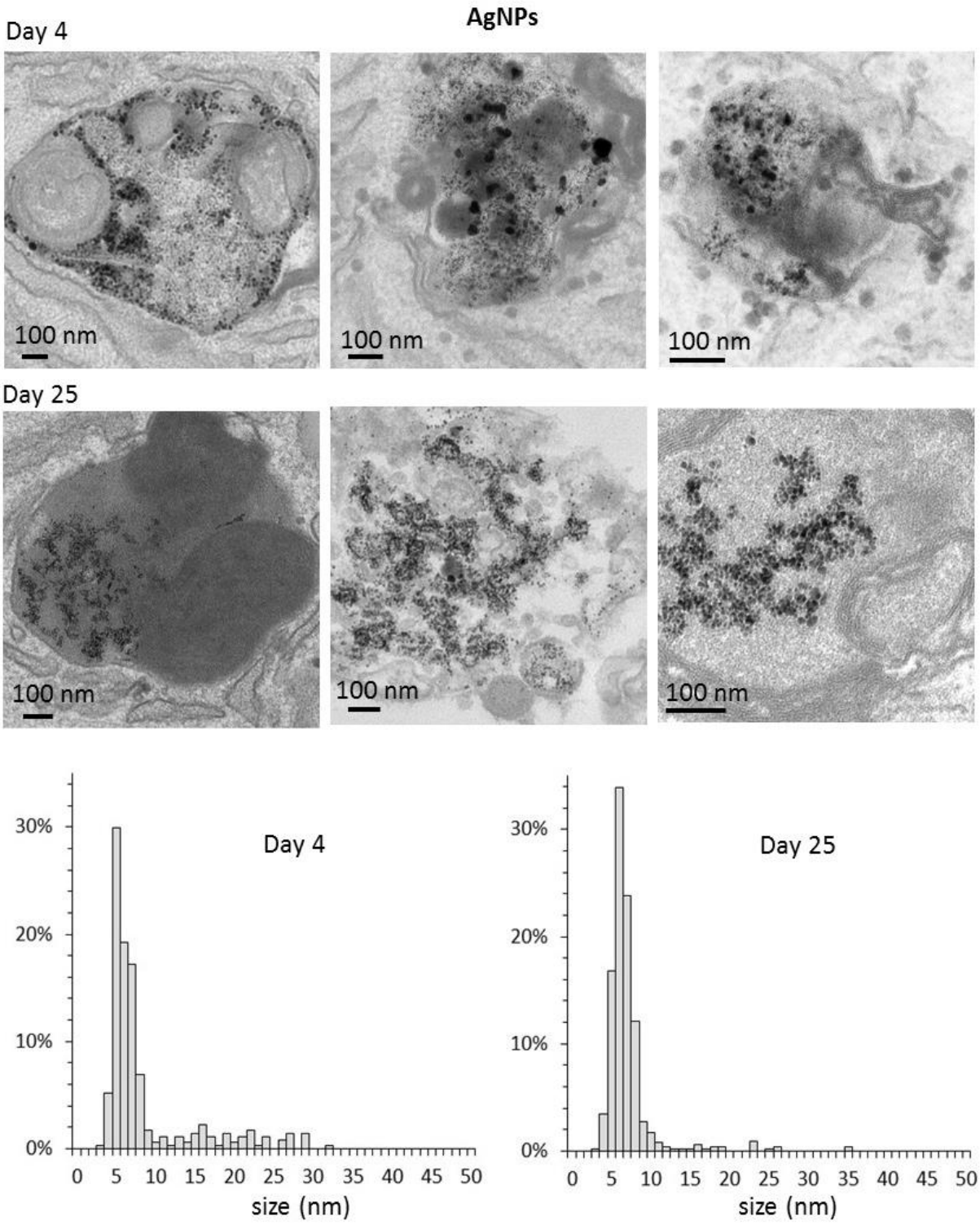

Figure S3. TEM micrographs of endosomes within MSC stem cells on days 4 and 25 after incubation with AgNPs. The sizes of NPs-like dark dots were measured. Two populations emerge. One centered at 6 nm, corresponding to the typical size of the ferritin cavity, the other shifted to larger sizes (beyond 10 nm). This second population correspond to 19% of the measured dots for the day 4 condition, and only to 5% of all measurements for the day 25 condition. Besides, the average size of this second population decrease from 20 nm at day 4 to 16 nm at day 25. It probably corresponds to remains of the initial NPs.

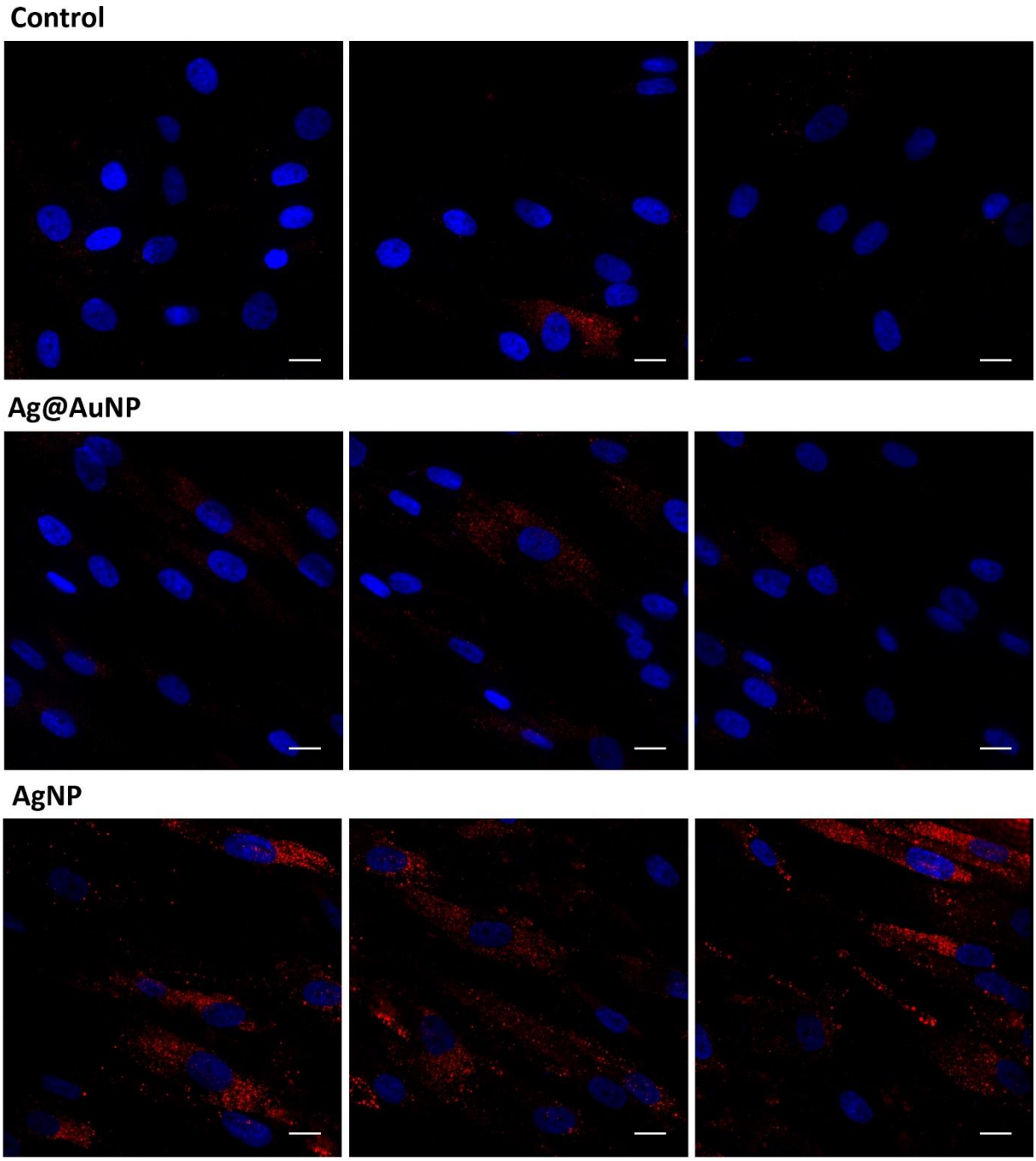

Figure S4. Immunostaining (in red) of the ferritin proteins in MSC cells, in control conditions (no NPs, top), with internalized non-degraded Ag@AuNPs (middle), and with internalized and degraded AgNPs (bottom). In the latter case, the ferritin protein is clearly overexpressed in the cells with degraded silver. Nuclear DAPI staining (in blue) is overlaid on all images. Scale bar: 20 μm.

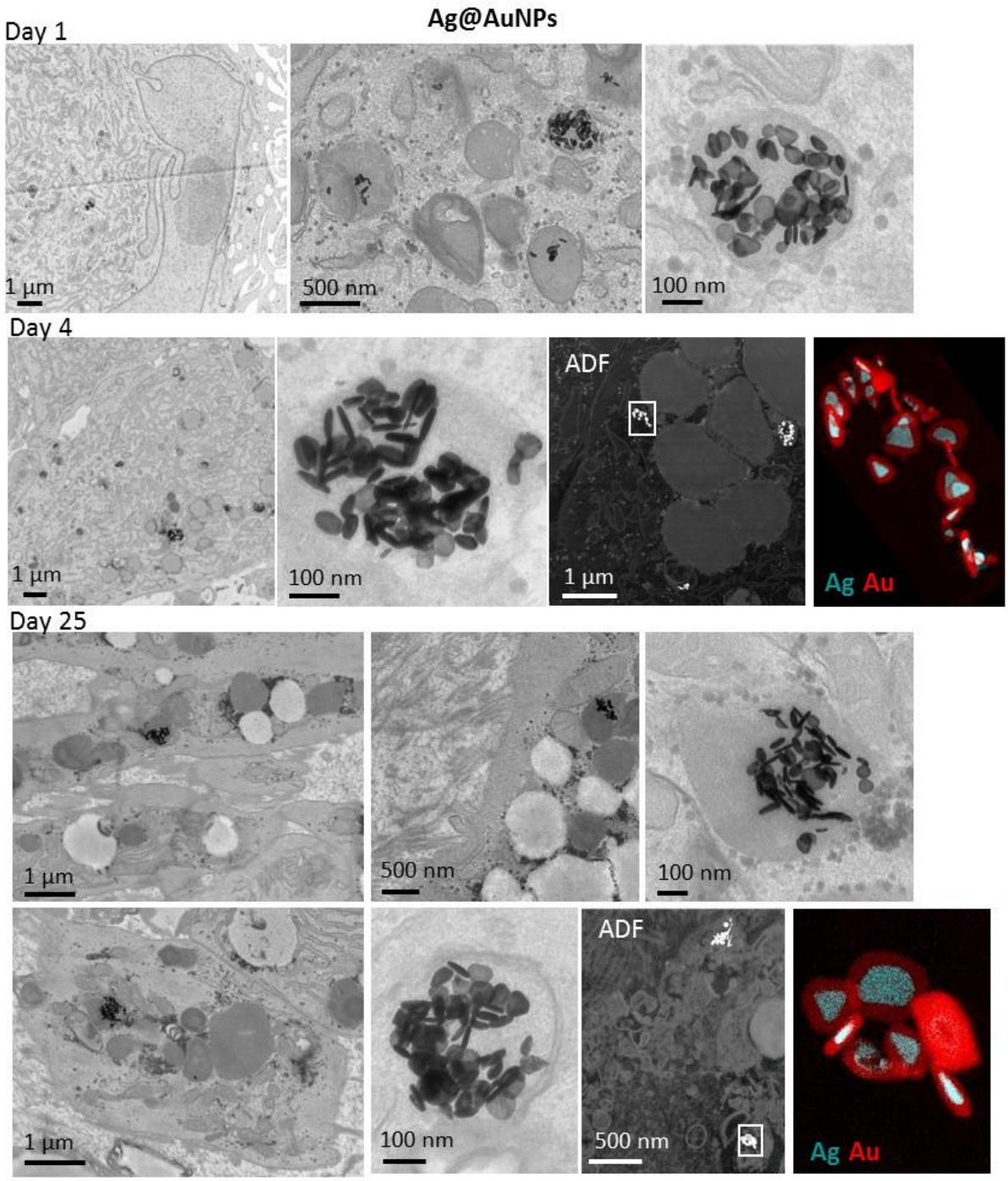

Figure S5. TEM micrographs of MSC stem cells on days 1, 4 and 25 after after incubation with Ag@AuNPs. Micrographs were acquired at different magnifications (scale bars 1 µm, 500 and 100 nm) to zoom on cell confinement into endosomes. At days 4 and 25 after incubation, ADF images and EELS elemental maps were also obtained, demonstrating clearly that the gold shell totally protects the Ag core. This shielding effect can be compared to similar Au protection of an iron oxide core[2].

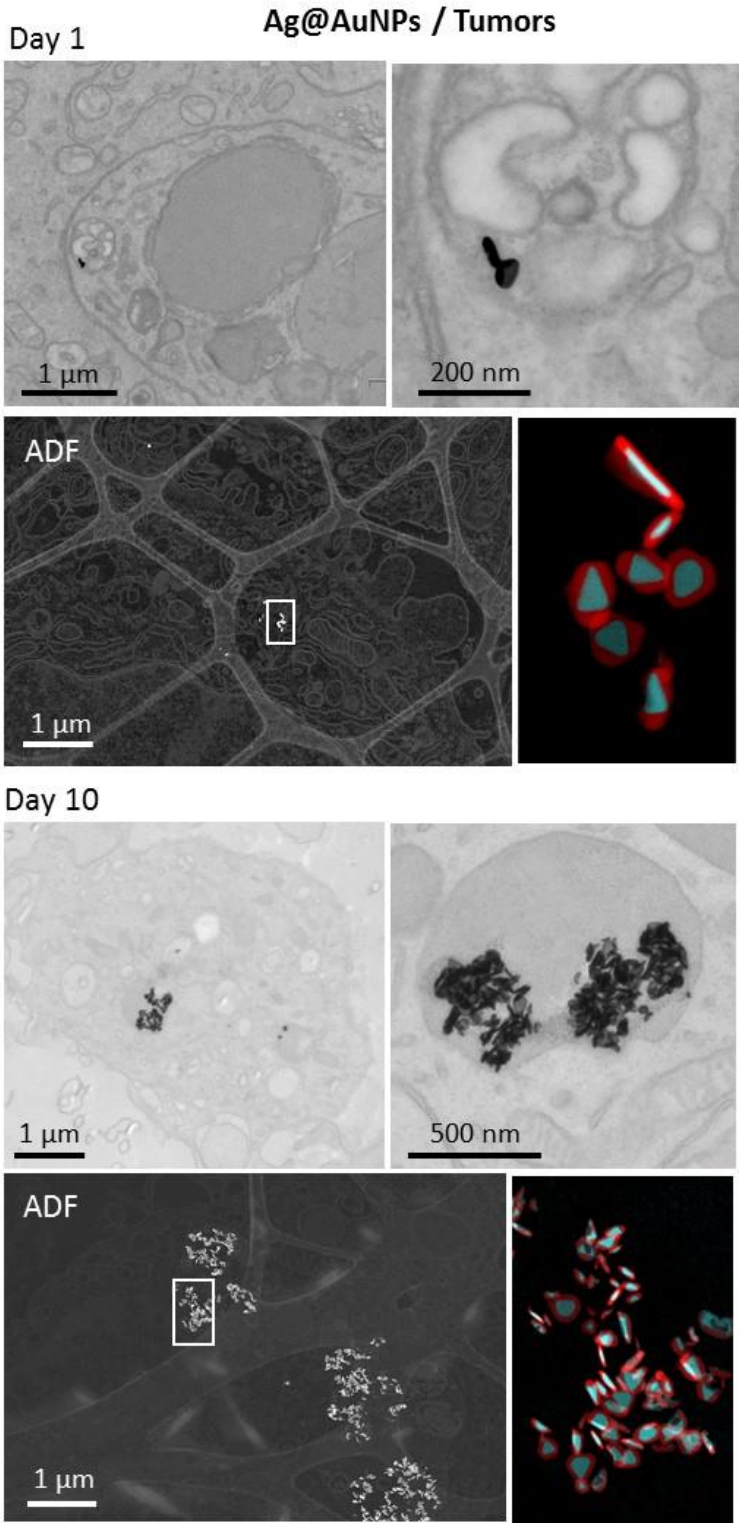

Figure S6. TEM micrographs, ADF images and EELS elemental maps of Ag@AuNP *in vitro* and *in vivo* in tumours at day 1 and 10 after intratumoral injection.

REFERENCES

1. Espinosa, A.; Silva, A. K.; Sánchez-Iglesias, A.; Grzelczak, M.; Péchoux, C.; Desboeufs, K.; Liz-Marzán, L. M.; Wilhelm, C., Cancer Cell Internalization of Gold Nanostars Impacts their Photothermal Efficiency *in Vitro* and *in Vivo*: Toward a Plasmonic Thermal Fingerprint in Tumoral Environment. *Adv. Healthcare Mater.* **2016,** *5*, 1040-1048.

2. Mazuel, F.; Espinosa, A.; Radtke, G.; Bugnet, M.; Neveu, S.; Lalatonne, Y.; Botton, G. A.; Abou-Hassan, A.; Wilhelm, C., Magneto-Thermal Metrics Can Mirror the Long-Term Intracellular Fate of Magneto-Plasmonic Nanohybrids and Reveal the Remarkable Shielding Effect of Gold. *Adv. Funct. Mater.* **2017,** *27*, 1605997.